

43 Antarctica (Rignot et al., 2013, Roberts et al., 2018) and has thinned and lost mass
44 rapidly in recent years (Pritchard et al., 2009; Adusumilli et al., 2020).

45

46 The ASB has a widespread distributed hydrological network with almost 200 ‘lake-like’
47 or water accumulation features: [\(Wright et al., 2012; Livingstone et al., 2022\)](#). There
48 may be a hydrological flow pathway operating from subglacial lakes near the Dome C
49 ice divide and the coast via the Totten Glacier (Wright et al., 2012), potentially affecting
50 the stability of the Totten Glacier.

51

52 Basal melting ~~may~~ contribute to subglacial hydrological flow. Basal meltwater
53 lubricates the flow of ice, which can impact the stability of the ice sheet and the
54 direction of the ice flow (Livingstone et al., 2016; Bell et al., 2007). The basal meltwater
55 moves down the pressure gradient and gradually develops into a complex subglacial
56 hydrological system, which eventually flows into the ocean (Fricker et al., 2016).
57 However, the spatial structure of the basal thermal state and basal melting rates beneath
58 the Totten Glacier are not yet well understood.

59

60 Basal melting can occur where the ice temperature reaches the pressure melting point,
61 dramatically lowering the basal friction and allowing the ice to flow faster. Geothermal
62 heat [fluxflow](#) (GHF) is [an importanta key](#) boundary condition for ice temperature. Its
63 magnitude and distribution affect the distribution of basal ice temperature and thus [the](#)
64 ice flow. The magnitude of GHF depends on the spatially varying geological conditions
65 that control heat generation and conduction, including heat [fluxflow](#) from the mantle,
66 crustal thickness, heat production in the crust by radioactive decay, groundwater flow,
67 and tectonic history (Pollack et al., 1993; Pittard et al., ~~2016~~; [2016; Reading et al.,](#)
68 [2022](#)). [The bed topography affects heat diffusion pathways to the earth’s crust, therefore](#)
69 [has influence on GHF at kilometer scales. Typically, near-surface temperature gradient](#)
70 [is decreased near topographic rises and increased near topographic depressions \(Bullard,](#)
71 [1938; Colgan et al., 2021\)](#). It is difficult to measure GHF directly due to limited access
72 to Antarctic bedrock, with only a few point measurements in ice-free areas or from
73 boreholes through the ice (Fisher et al., 2015). GHF datasets are commonly estimated
74 from models ([Burton-Johnson et al., 2020](#)) relying on either seismic [models](#) (Shapiro
75 and Ritzwoller, 2004; An et al., 2015; Shen et al., 2020), ~~airborne magnetic~~
76 ~~data~~ [magnetically-derived models](#) (Martos et al., 2017), ~~or satellite geomagnetic data~~ ([;](#)
77 [Purucker, 2012 - an update of](#) Fox-Maule et al., 2005; ~~Purucker et al., 2013~~); ~~or~~
78 [multivariate approach \(Stål et al., 2021\) including machine learning \(Lösing et al.,](#)
79 [2021\)](#).

80

81 Previous thermomechanical simulations of [the whole Antarctic including](#) Totten Glacier
82 (Dow et al., 2020; Pattyn et al., 2010; Pittard et al., 2016; Van ~~Liefferinge~~ [Liefferinge](#)
83 [and Pattyn, 2013; Van Liefferinge](#) et al., 2018) have used GHF data from Shapiro and
84 Ritzwoller (2004), [Fox Maule et al. \(2005\)](#), Purucker ~~et al. (2013)~~ [\(2012\)](#) and An et al.
85 (2015), but Wright et al. (2012) [and Huybrechts \(1990\)](#) used spatially uniform values.
86 In this study, we simulated the basal thermal state of Totten Glacier, based on the best

87 available topographic data and ~~five~~eight different GHFs, including three GHF listed
88 above, plus more recent GHF fields from Martos et al. (2017) and Shen et al.
89 ~~(2020)~~(2020), and three latest GHF datasets from Stål et al. (2021), Lösing et al. (2021),
90 ~~and Haeger et al. (2022)~~.

91
92 We apply an off-line coupling between a basal energy and water flow model and a 3D
93 full-Stokes ice flow model for each of the ~~five~~eight GHF maps, to provide the best-fit
94 distribution of modelled basal temperature and basal melt rate. We evaluate the
95 simulated basal temperature fields under the different GHF maps using the observations
96 of water at the ice base to infer which GHF map is most reliable in the ASB. The
97 observations include a set of subglacial lakes locations and the specular content (Dow
98 et al., 2020) calculated from airborne radar data collected by the International
99 Collaborative Exploration of the Cryosphere by Airborne Profiling (ICECAP) survey.
100 Specularity is a parameterization of the along-track radar bed reflection scattering
101 function that has been used to provide an attenuation-independent proxy for distributed
102 subglacial water bodies (Schroeder et al., 2013). We devise measures of specularity that
103 help discriminate between alternative GHF maps to best characterize both cold and
104 warm beds.

105 106 **2 Regional Domain and Datasets**

107 Our modeled domain, the Totten Glacier, is located in the Aurora Subglacial Basin in
108 East Antarctica (Fig. 1). Its boundary is based on drainage-basin boundaries defined
109 from satellite ice sheet surface elevation and velocities (Mouginot et al., 2017). The
110 surface elevation, bedrock elevation, and ice thickness are from MEaSURES
111 BedMachine Antarctica, version 2 with a resolution of 500 m (Morlighem et al., 2020).

112
113 Simulation input and comparison datasets are shown in Table 1. The surface ice velocity
114 data are obtained from MEaSURES Phase-Based Antarctica Ice Velocity Map, Version
115 2 with resolution of 450 m (Rignot et al., 2017), which were mainly collected during
116 the International Polar Years from 2007 to 2009 with additional surveys between 2013
117 and 2016. Ice sheet surface temperature is prescribed by ALBMAP v1 with a resolution
118 of 5 km (Le Brocq et al., ~~2010~~2010a) and comes from monthly estimates inferred from
119 AVHRR data averaged over 1982-2004 (Comiso, 2000). Subglacial lake locations are
120 from the fourth inventory of Antarctic subglacial lakes (Wright and Siegert, 2012) and
121 the first global inventory of subglacial lakes (Livingstone et al., 2022).

122
~~123 Five GHF datasets (Fig. 2; Table 2) are used in this study. All the datasets are~~
124 ~~interpolated into 2.0 km resolution. Eight GHF datasets (Fig. 2; Table 2) are used in this~~
125 ~~study. Martos et al. (2017) GHF and Purucker (2012) GHF are both derived from~~
126 ~~magnetically-derived models, but their magnitude vary significantly on a regional scale,~~
127 ~~which is mainly related to the resolution of magnetic anomaly data (Burton-Johnson et~~
128 ~~al., 2020). Shapiro and Ritzwoller (2004), An et al. (2015), and Shen et al. (2020) all~~
129 ~~used seismic data, but they used different approaches in deriving heat flow. The latest~~
130 ~~three GHF datasets, Stål et al. (2021), Lösing et al. (2021), and Haeger et al. (2022), are~~

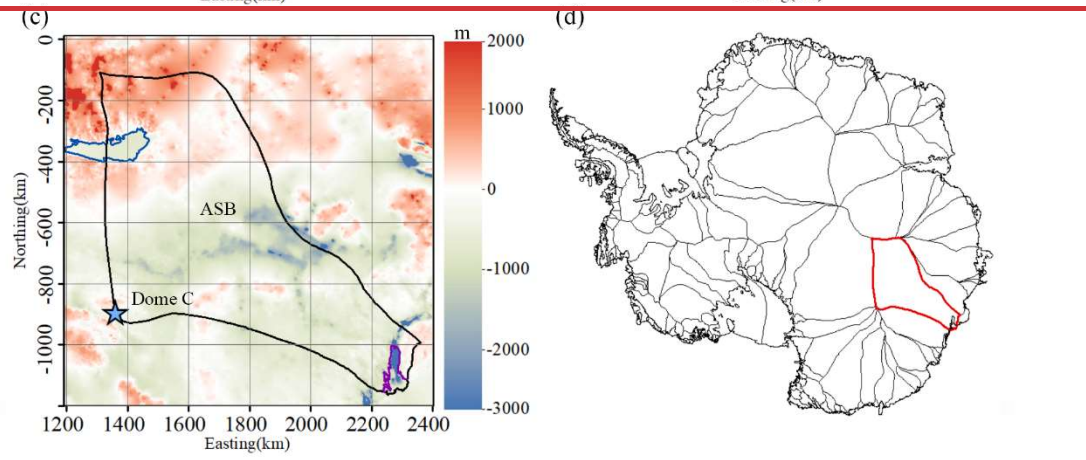
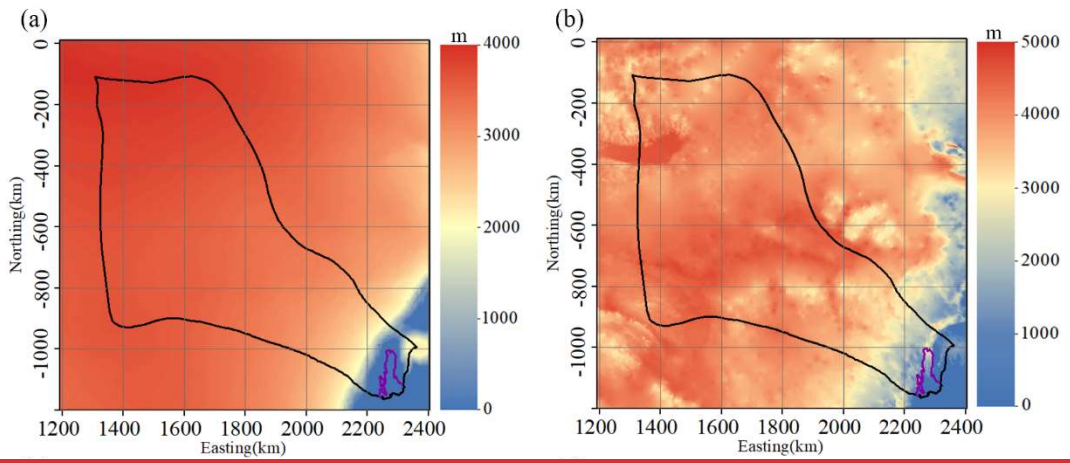
131 generated based on multiple observables. All the GHF datasets are bilinearly
 132 interpolated into 2.0 km resolution. Then we calculated the ensemble mean and standard
 133 deviation (SD) of the eight GHF maps, and a uniform GHF value, 59 mW m^{-2} , which
 134 is the area average of ensemble mean (Fig. 2). The SD of 8 GHF is less than 10 mW m^{-2}
 135 over the domain.

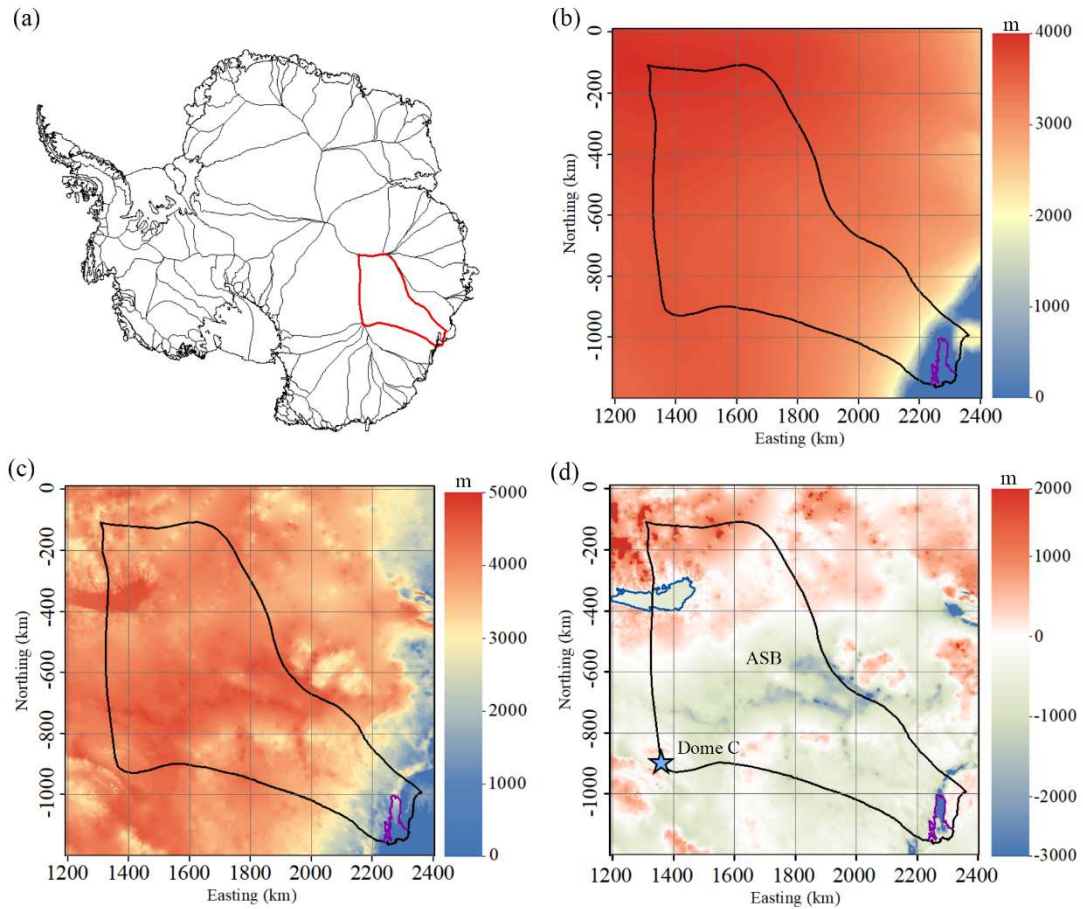
136
 137 The specularity content data are from Dow et al (2020), where they calculated radar
 138 specularity content over ASB from the ICECAP survey lines, and smoothed the data
 139 with a 1 km filter, following the equations described in Schroeder et al. (2015).
 140 Specularity content is given as a relative value between 0 and 1, larger values mean a
 141 higher likelihood of ~~thewater~~ presence-of-water, and value of 0.4 is taken as the division
 142 where specularity content shows the presence of water (Young et al., 2016).

143

144 Table 1 Datasets used in simulations.

Variable name	Dataset	Resolution	Reference
surface elevation, bedrock elevation, and ice thickness	MEaSURES BedMachine Antarctica version 2	500 m	Morlighem et al., 2020; Cui et al., 2020
surface ice velocity	MEaSURES InSAR-based Antarctic ice velocity Map, version 2	450 m	Rignot et al., 2017
surface temperature	ALBMAP v1	5 km	Le Brocq et al., 2010 2010a
subglacial lake location	The first global inventory of subglacial lakes	-----	Wright and Siegert, 2012; Livingstone et al., 2022
specularity content	Aurora Subglacial Basin GlaDs inputs, outputs and geophysical data	1 km along track	Dow et al., 2019





147

148 Fig. 1. The domain topography and location with domain boundary overlay. (a) surface elevation;
 149 (b) ice thickness; (c) bed elevation; (d) the location of our domain in Antarctica; (b) surface
 150 elevation; (c) ice thickness; (d) bed elevation with region boundary overlay. The solid black curve
 151 is the outline of the study domain, including the Totten ice shelf. The solid red line in (a) is the
 152 boundary of Totten Glacier. The purple curve in (a-e) depicts the grounding line of Totten
 153 glacier. The blue curve in (e) depicts Lake Vostok (Studinger et al., 2003). The solid red curve
 154 in (d) is the boundary of Totten Glacier. ASB and Dome C (blue star) are marked in (ed).

155

156

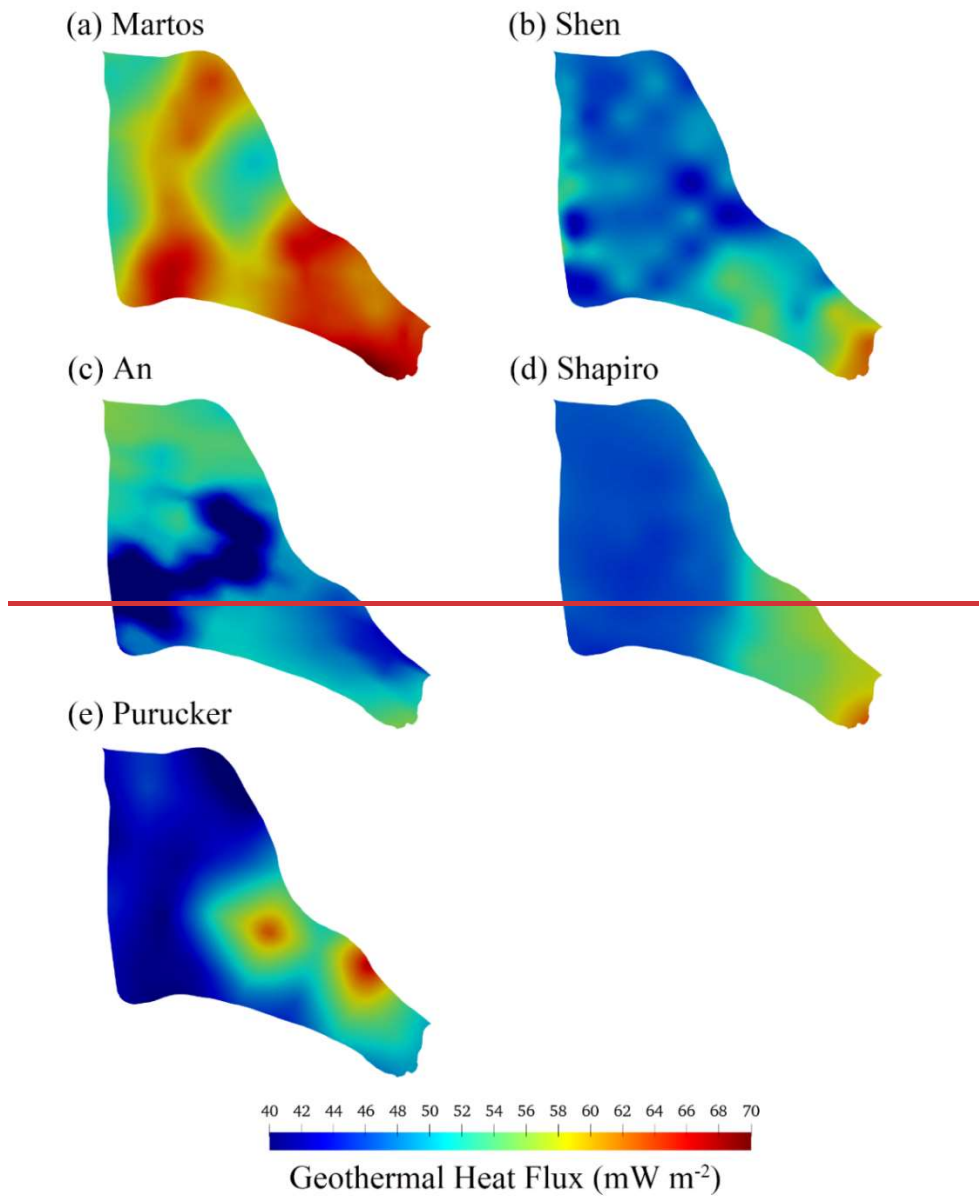
157

158 Table 2 The five GHF datasets used with the mean and range and resolution in
 159 our region.

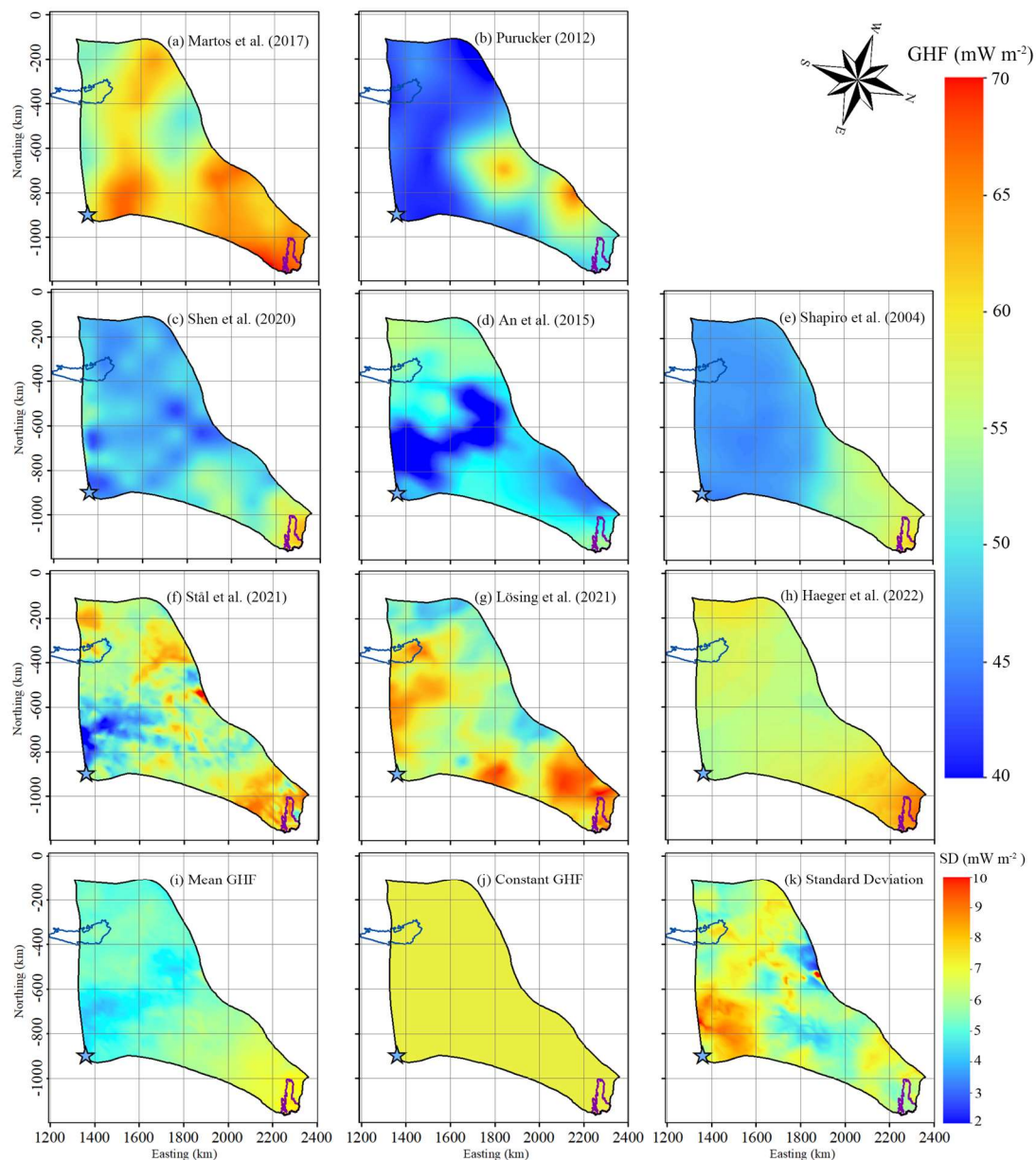
160

GHF <u>maps</u>	<u>Method</u> <u>Reference</u>	<u>Mean</u> <u>(mW m⁻²)</u> <u>Method</u>	<u>Mean-</u> <u>Range</u> <u>(mW m⁻²)</u>	<u>Range</u> (mW m ⁻²) <u>Resolution</u> <u>(km)</u>
<u>Martos et al., 2017</u>	<u>Martos et al., 2017</u> <u>airborne geomagnetic</u> <u>data derived model</u>	<u>airborne</u> <u>geomagnetic</u> <u>data</u> <u>65</u>	<u>65-70</u>	<u>51-70</u> <u>15</u>
<u>Purucker, 2012</u>	<u>satellite geomagnetic</u> <u>data derived model</u>	<u>51</u>	<u>37-67</u>	<u>100-400</u>
<u>Shen et al., 2020</u>	<u>seismic model</u> <u>Shen et al., 2020</u>	<u>seismic</u> <u>model</u> <u>58</u>	<u>58-63</u>	<u>42-63</u> <u>100-200</u>

An et al., 2015	seismic model An et al., 2015	51 seismic model	34-56 51	100-200 34-56
Shapiro and Ritzwoller, 2004	Shapiro and Ritzwoller, 2004 seismic model	58 seismic model	58 44-63	44-63 ~100
Stål et al., 2021	multivariate approach	60	34-80	20
Lösing et al., 2021	machine learning	63	47-71	55
Purucker Haeger et al., 2022	Purucker, 2013 multivariate approach	Satellite geomagnetic data 64	51-54-67	103-67
Mean GHF	Ensemble mean of the 8 datasets above interpolated into 2.0 km resolution	59	48-61	2
Constant GHF	mean of the ensemble mean GHF	59	59	2



161
162
163



164

165 Fig. 2. The spatial distribution of GHF listed in Table 2 over our domain as described in Fig. 1. See
 166 Table 2 for (a)-(j). The ensemble mean GHF and standard deviation of the GHF map details GHF
 167 (a)-(h) are given in (i) and (k). Panel (j) shows the constant GHF of 59 mW m^{-2} . The purple line
 168 depicts the grounding line. The blue curve depicts Lake Vostok. The blue star denotes Dome C.

169

170 3 Model

171 Our goal is to map the basal thermal state of Totten glacier, including basal temperature
 172 and basal melting rate. GHF, basal frictional heat and englacial heat conduction are the
 173 main factors that determine the basal thermal state of the ice sheet. We need to simulate
 174 the ice flow velocity and stress to calculate the basal frictional heat, and to simulate the
 175 ice temperature to calculate the englacial heat conduction flux.

176

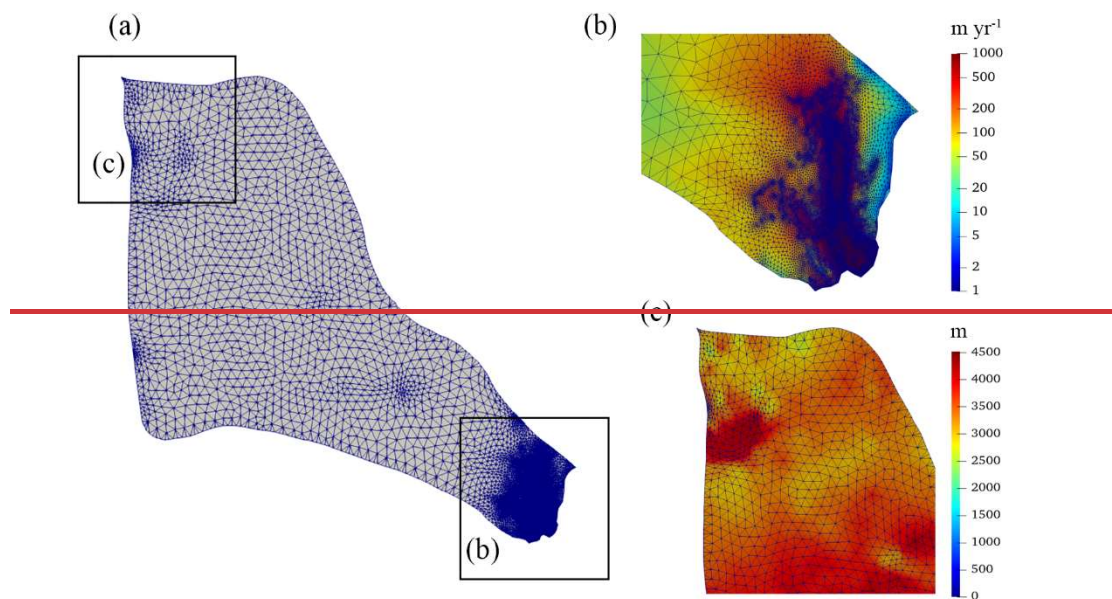
177 Following the same method as Kang et al. (2022), we solve an inverse problem by a
 178 full-Stokes model, implemented in Elmer/Ice, (Gagliardini et al., 2013), to infer the

179 basal friction coefficient such that the modelled velocity best fits observations. To get
180 a proper vertical ice temperature profile subject to thermal boundary conditions needed
181 in solving the inverse problem, we use a forward model that consists of an improved
182 Shallow Ice Approximation (SIA) thermomechanical model with a subglacial
183 hydrology model (Wolovick et al., [2021a](#)[2021](#)). We do steady state simulations by
184 coupling the forward and inverse models—, using 8 GHF datasets, as well as the
185 ensemble mean GHF and a constant GHF value of 59 mW m^{-2} (Fig. 2).

186

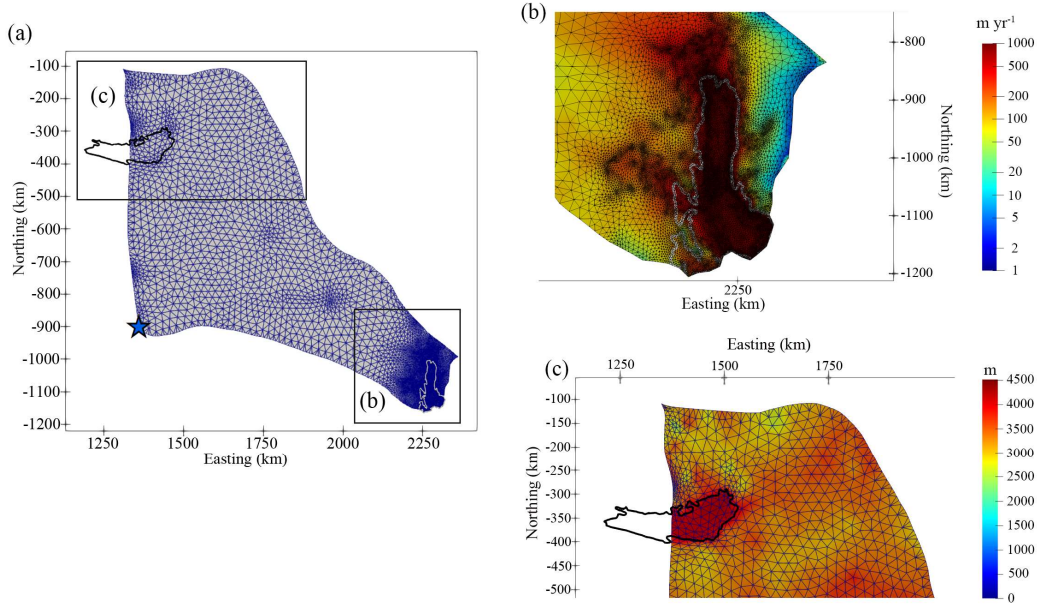
187 3.1 Mesh Generation and Refinement

188 We use GMSH (Geuzaine and Remacle, 2009) to generate an initial 2-D horizontal
189 footprint mesh. Then we refine the mesh by an anisotropic mesh adaptation code in the
190 Mmg library (<http://www.mmgtools.org/>). The resulting mesh is shown in Fig. 3 and
191 has minimum and maximum element sizes of about 800 m and 20 km. The range of
192 mesh size is 800 m at ice shelf, 1-3 km upstream near the grounding line, and 6-20 km
193 over most of the inland ice. The 2-D mesh is then vertically extruded using 10 equally
194 spaced, terrain following layers.



195

196



197

198 Fig. 3. The refined 2-D horizontal domain footprint mesh (a). Boxes outlined in (a) are shown in
 199 detail overlain with surface ice velocity (unit: m yr^{-1}) in (b) and with ice thickness in (c). The while
 200 line in (a) and (b) depicts the grounding line. The black curve in (a) and (c) depicts Lake Vostok.
 201 The blue star in (a) denotes Dome C.

202

203 3.2 Boundary Conditions

204 The ice surface is assumed to be stress-free. At the ice front, the normal stress under the
 205 sea surface is equal to the hydrostatic water pressure. On the lateral boundary, the
 206 normal stress is equal to the ice pressure applied by neighboring glaciers and the normal
 207 velocity is assumed to be 0. The bed for grounded ice is assumed to be rigid,
 208 impenetrable, and fixed over time. For simplicity, we ignore the existence of Lake
 209 Vostok and replace the lake with bedrock. We do this to avoid having to implement a
 210 spatially variable sea level in our model, as the level of hydrostatic equilibrium in Lake
 211 Vostok is several thousand meters higher than in the ocean. Our inverted drag
 212 coefficient over the lake is very low, indicating that our simplification has only a small
 213 influence on ice flow. However, our basal melt rates over the lake are probably
 214 inaccurate, as we assume that geothermal flux from the lake bottom is applied directly
 215 to the ice base, without accounting for circulation within the lake.

216 A linear sliding law is used to describe the relationship between the basal sliding
 217 velocity and the basal shear force, on the bottom of grounded ice,

$$\tau_b = C \cdot u_b, \quad (1)$$

218 To avoid non-physical negative values, $C = 10^\beta$ is used in the simulation. We call β
 219 the basal friction coefficient. C is initialized to a constant value of $10^{-4} \text{ MPa m}^{-1} \text{ yr}$
 220 (Gillet-Chaulet et al., 2012), and then replaced with the inverted C in subsequent
 221 inversion steps.

222

223 We relax the free surface of the domain by a short transient run to reduce the non-

224 physical spikes in initial surface geometry (Zhao et al., 2018). The transient simulation
225 period here is 0.5 yr with a timestep of 0.01 yr.

226

227 Following the same method as Kang et al. (2022), we improve the parameterization of
228 β via C in Eq 5 (Section 3.2.2) by considering basal temperature T_{bed} ,

$$\beta_{new} = \beta_{old} + \alpha(T_m - T_{bed}), \quad (2)$$

229 where β_{old} is from the inverse model, α is a positive factor to be tuned, T_m is pressure
230 melting temperature. We take α to be 1, and use the parameterization of β_{new} in Eq 1
231 in all the simulations (Kang et al., 2022). Using Eq 2 does not change simulated surface
232 velocities in the interior region.

233

234 **3.3 Basal Melt Rate**

235 Based on the inverted basal velocity and basal shear stress, we can calculate the basal
236 friction heat. We then produce the basal melt rate using the thermal equilibrium as
237 follows (Greve and Blatter, 2009):

$$M = \frac{G + \bar{u}_b \bar{\tau}_b + k(T) \frac{dT}{dz}}{\rho_i L}, \quad (3)$$

238 where M is the basal melt rate, G is GHF, $\bar{u}_b \bar{\tau}_b$ is the basal friction heat, $-k(T) \frac{dT}{dz}$ is the

239 upward heat conduction, ρ_i is the ice density, and L is latent heat of ice melt. GHF and
240 frictional heating from basal slip warm the base, while the upward heat conduction to
241 the interior cools the base.

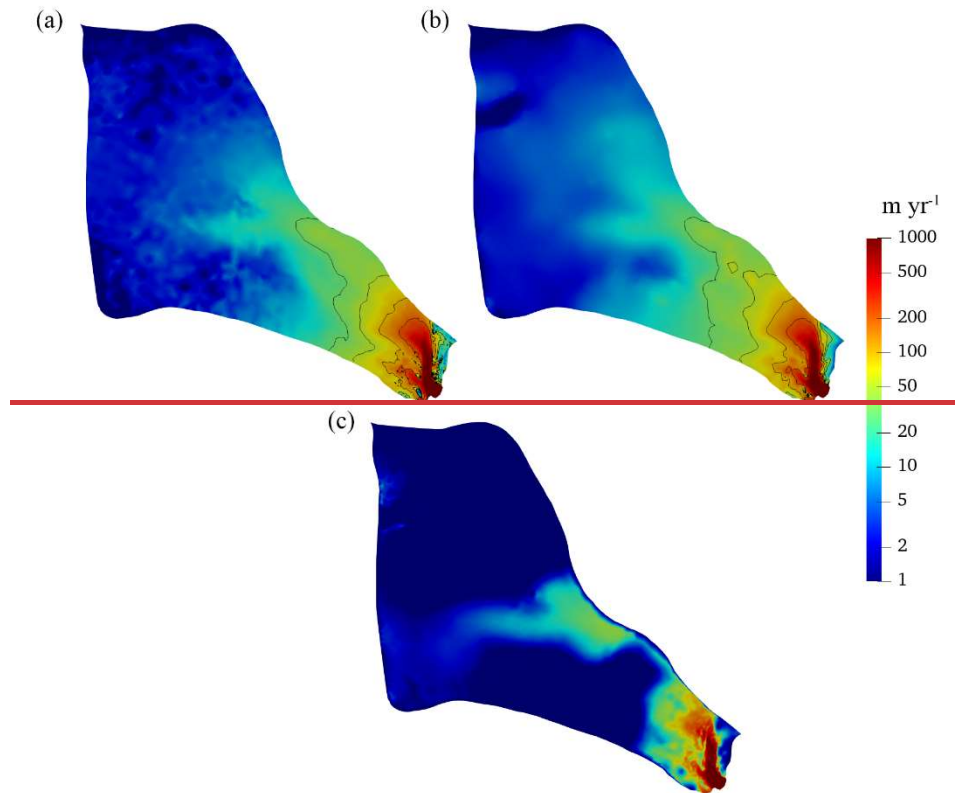
242 **4 Simulation Results**

243 **4.1 Ice Velocity**

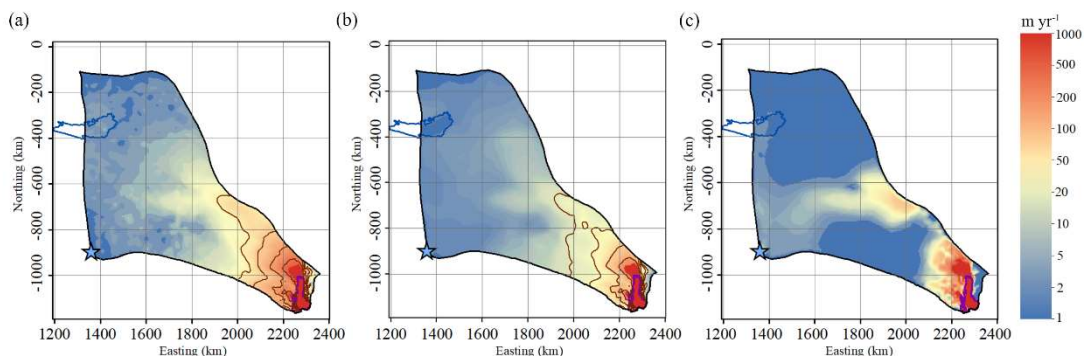
244 The modeled surface velocity fields with different GHFs are all very close to the
245 observed as expected by design of the minimization of misfit between the modeled and
246 the observed surface velocity in the inverse model. Therefore, we show only the Martos
247 et al. (2017) result as a representative example of all simulated velocity fields (Fig. 4).
248 The surface speed can reach as high as about 1000 m yr⁻¹ on the ice shelf (Fig. 4a, b).

249

250 Fig. 4c shows the modeled basal ice velocity. The modeled basal ice velocity is close to
251 0 in most of the inland region. The fast basal velocity in the middle of the region (Fig.
252 4c) is associated with subglacial canyon features (Fig. 1c), high basal temperature (Fig.
253 5) and small friction coefficient. In the grounded fast flow region, the basal ice velocity
254 can reach a maximum of 500 m yr⁻¹.



255
256



257

258 Fig. 4. (a) Observed surface velocity, (b) modeled surface velocity, and (c) modeled basal velocity
 259 in the experiment using the Martos et al. (2017) GHF. The black solid lines in (a) and (b)
 260 represent speed contours of 30, 50, 100 and 200 m yr⁻¹. The purple line depicts the grounding line.
 261 The blue curve depicts Lake Vostok. The blue star denotes Dome C.

262

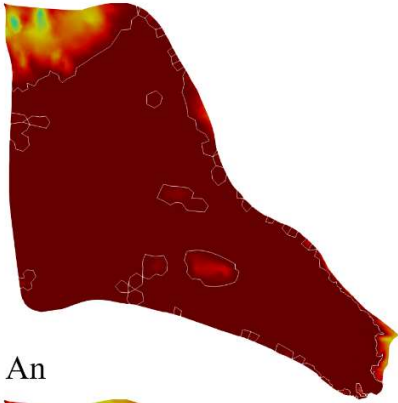
263 4.2 Basal Ice Temperature, Basal Friction Heat and Heat Conduction

264

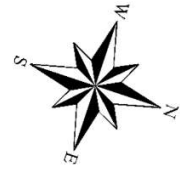
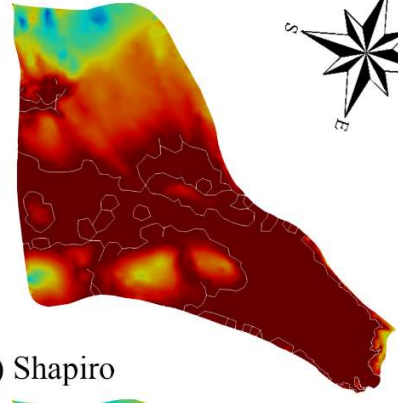
265 Fig. 5 shows the modelled basal temperatures from the five experiments. In the fast-
 266 flowing region (defined as having surface speeds higher than 30 m yr⁻¹), the modelled
 267 ice basal temperatures are all at the pressure melting point (“warm”). However, in the
 268 slow-flowing region, the modeled ice basal temperature shows large difference between
 269 GHF fields. In the experiment using the Martos et al. (2017), Haeger et al. (2022), Stål
 270 et al. (2021), and Lösing et al. (2021) GHF (Fig. 5a5), which has the highest similar high
 271 GHF over the domain, we get the largest area of warm base extending to all but the
 inland southeast-southwest corner. The warm bed yielded by the constant GHF is close

272 to the above four GHF, although the constant GHF value is lower than the mean value
273 of any one of the above four GHF (Table 2). The experiment using Shen et al. (2020)
274 GHF (Fig. 5b5c), which has the second highest/moderately high GHF, yields the second
275 largest/medium-sized area of warm base. The experiments using An et al. (2015),
276 Shapiro and Ritzwoller (2004) and Purucker (2012) GHF produce slightly less area of
277 warm bed than Shen et al. (2020) GHF. The experiment using Purucker ~~et al.~~
278 ~~(2013)~~(2012) GHF (Fig. 5e5b), with the lowest GHF has the smallest warm base area,
279 which is mostly confined to the fast-flowing region. All experiments show cold basal
280 temperatures in the southwest corner which is associated with relatively thin ice above
281 subglacial mountains (Fig. 4e).1c), and coincide with high values of SD in modelled
282 basal temperature (Fig. 5k). The warm bed area using the ensemble mean GHF is
283 between that by the top four high GHF, and that by Shen et al. (2020) GHF.

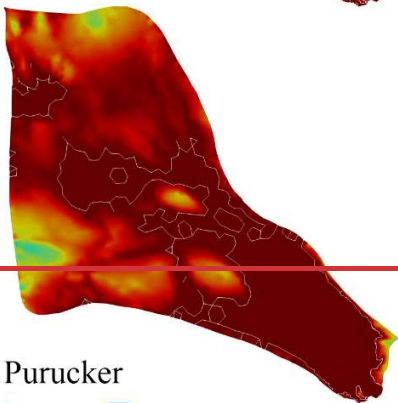
(a) Martos



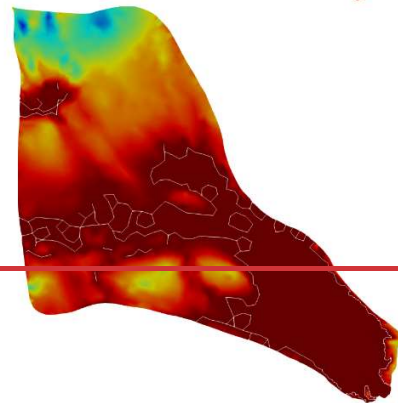
(b) Shen



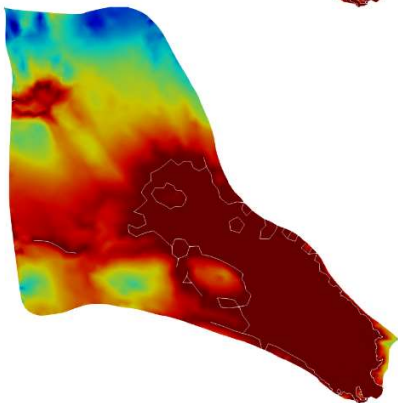
(c) An



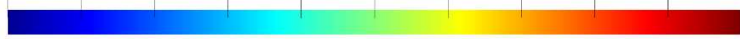
(d) Shapiro



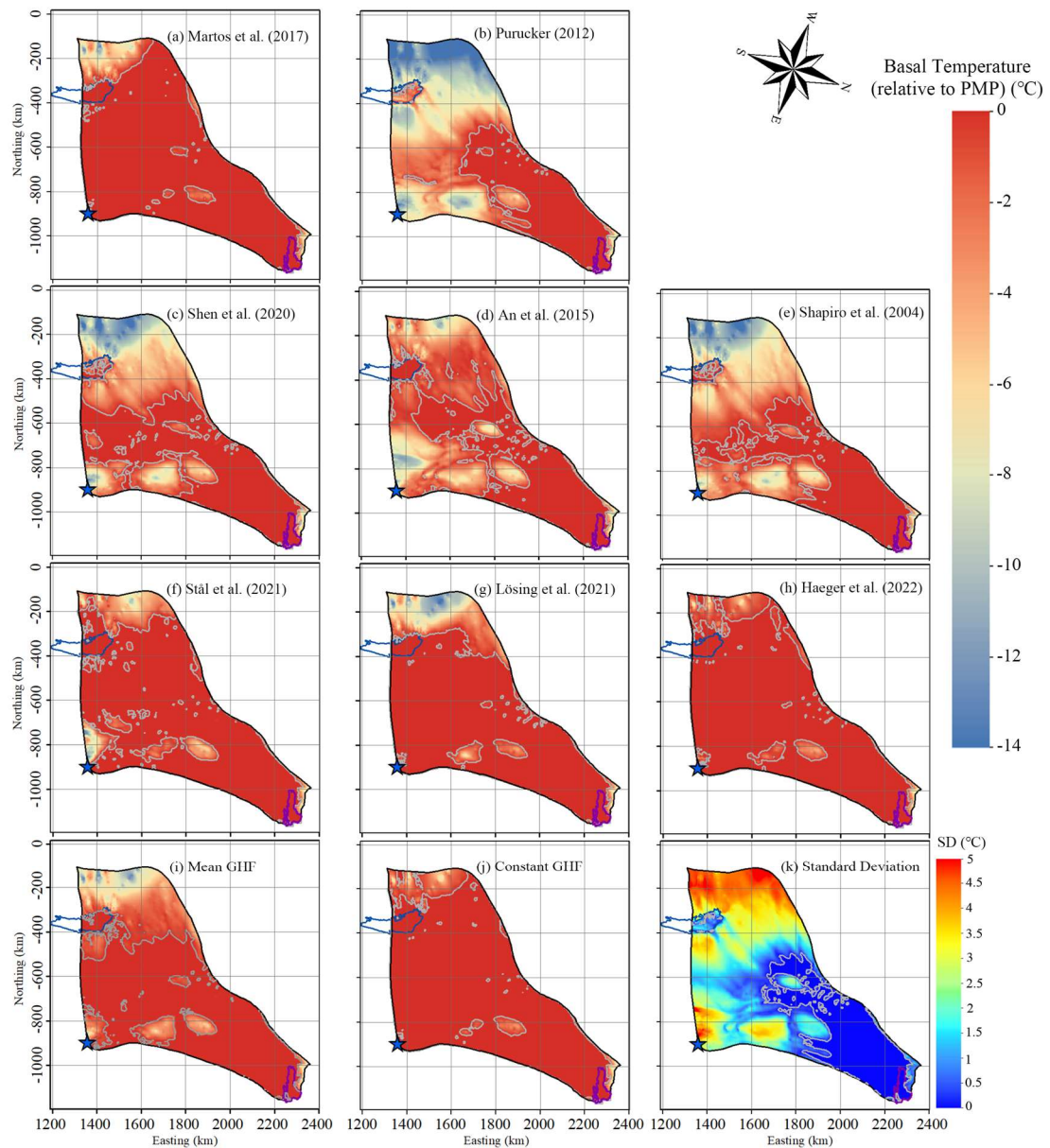
(e) Purucker



-20 -18 -16 -14 -12 -10 -8 -6 -4 -2 0



Basal Temperature (relative to PMP) (°C)



285

286

287

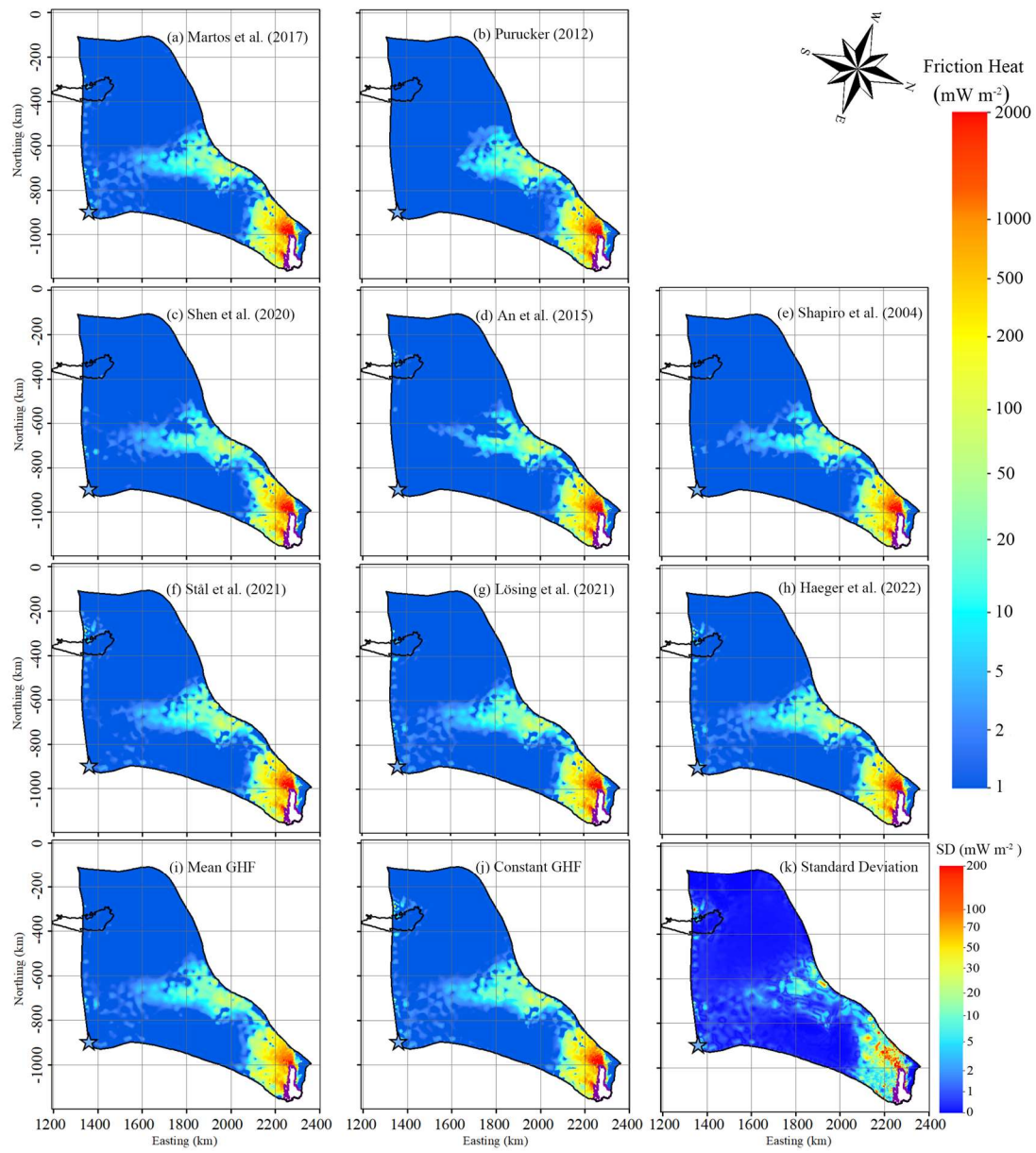
288

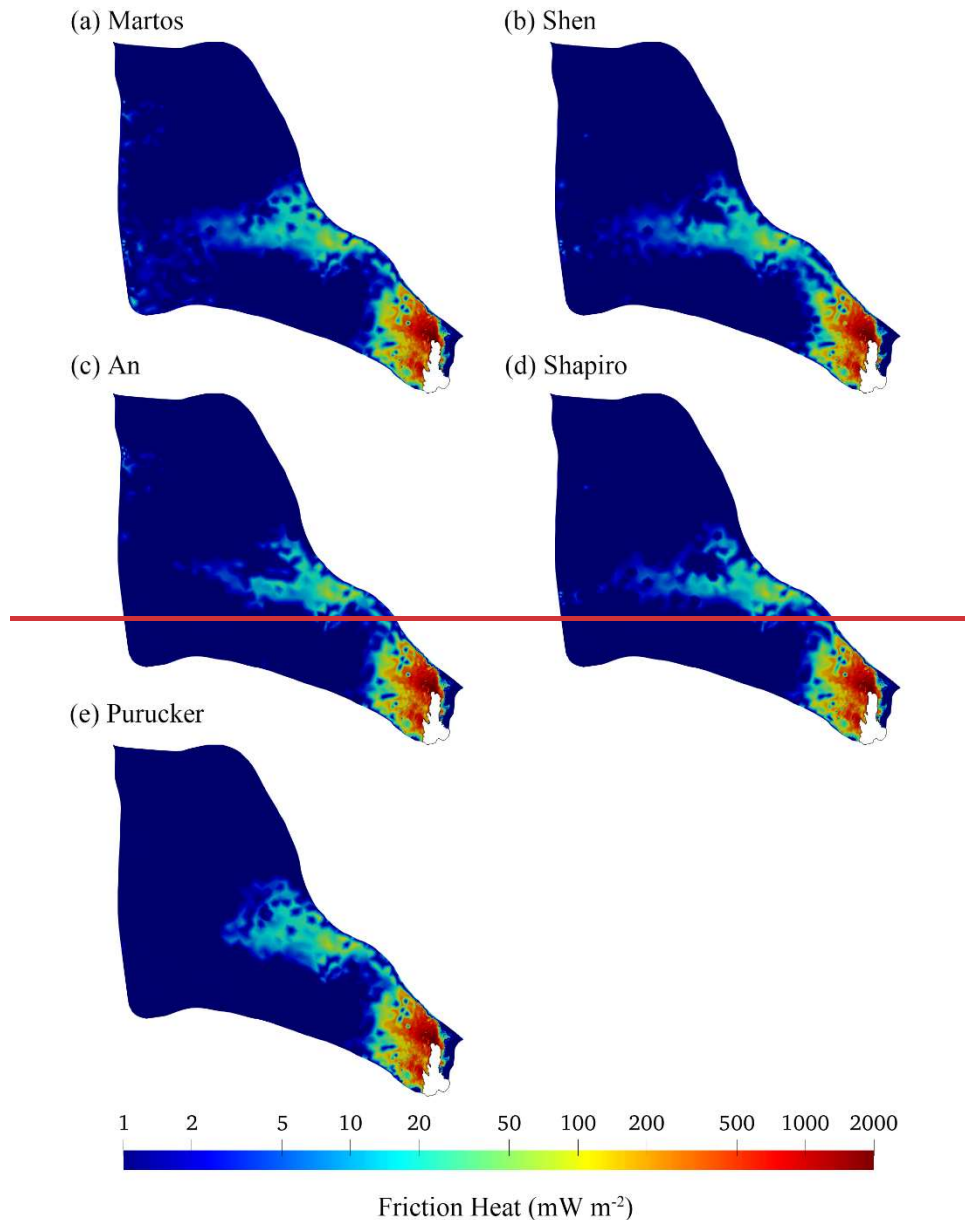
289

290

291

Fig. 5. Modelled basal temperature relative to pressure melting point, (a) to (e) corresponding to the GHF (a) to (e) in Fig. 2-2. Panel (k) is the standard deviation of 8 modelled basal temperatures (a)-(h). The ice bottom at the pressure-melting point is delineated by a whitegray contour. The purple line depicts the grounding line. The blue curve depicts Lake Vostok. The blue star denotes Dome C.



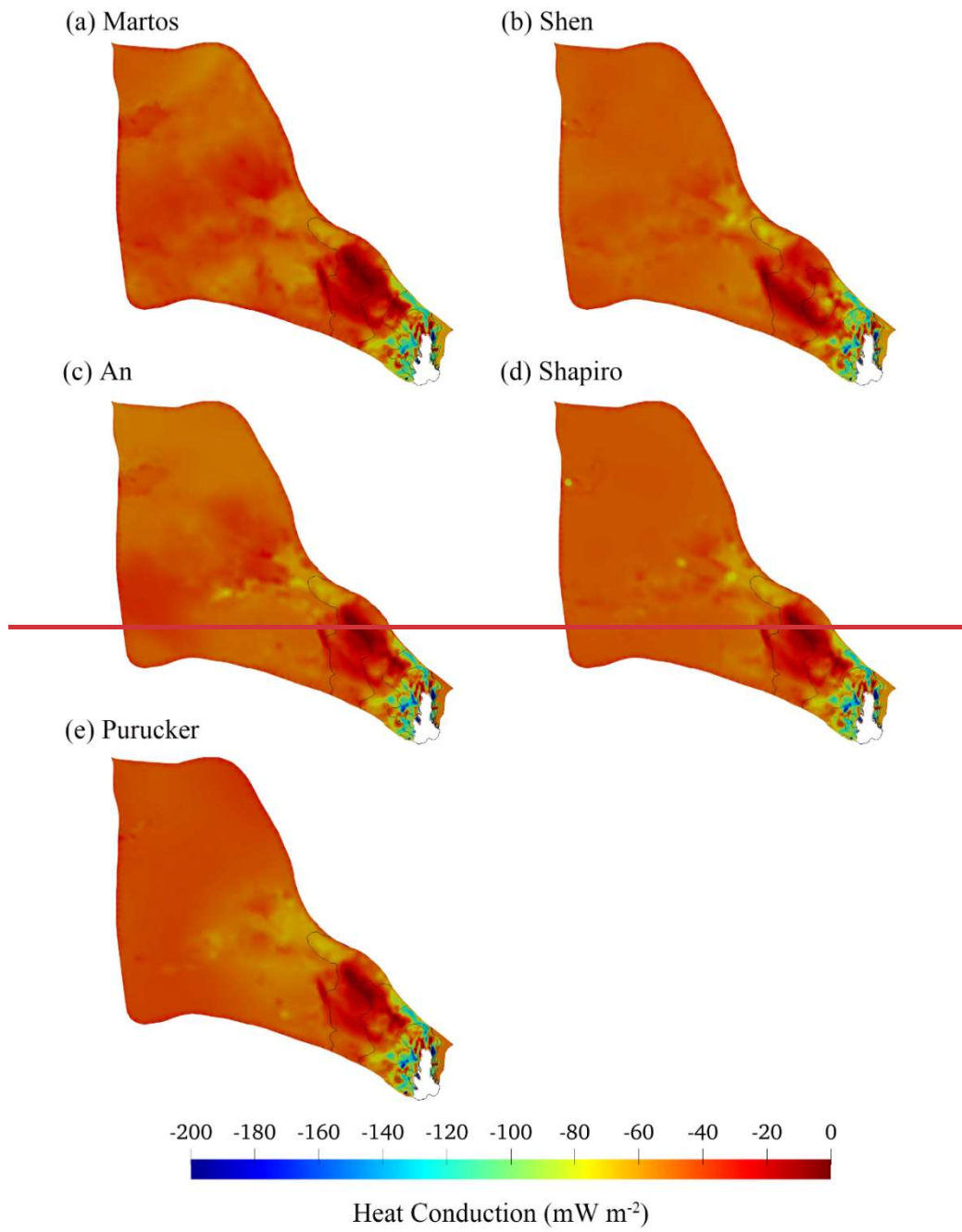


293 Fig.
 294 Fig. 6. Modelled basal friction heat.
 295 6. Modelled basal friction heat, (a) to (j) corresponding to the GHF (a) to (j) in Fig. 2. Panel (k) is
 296 the standard deviation of 8 modelled basal friction heat (a)-(h). The purple line depicts the grounding
 297 line. The black curve depicts Lake Vostok. The blue star denotes Dome C.

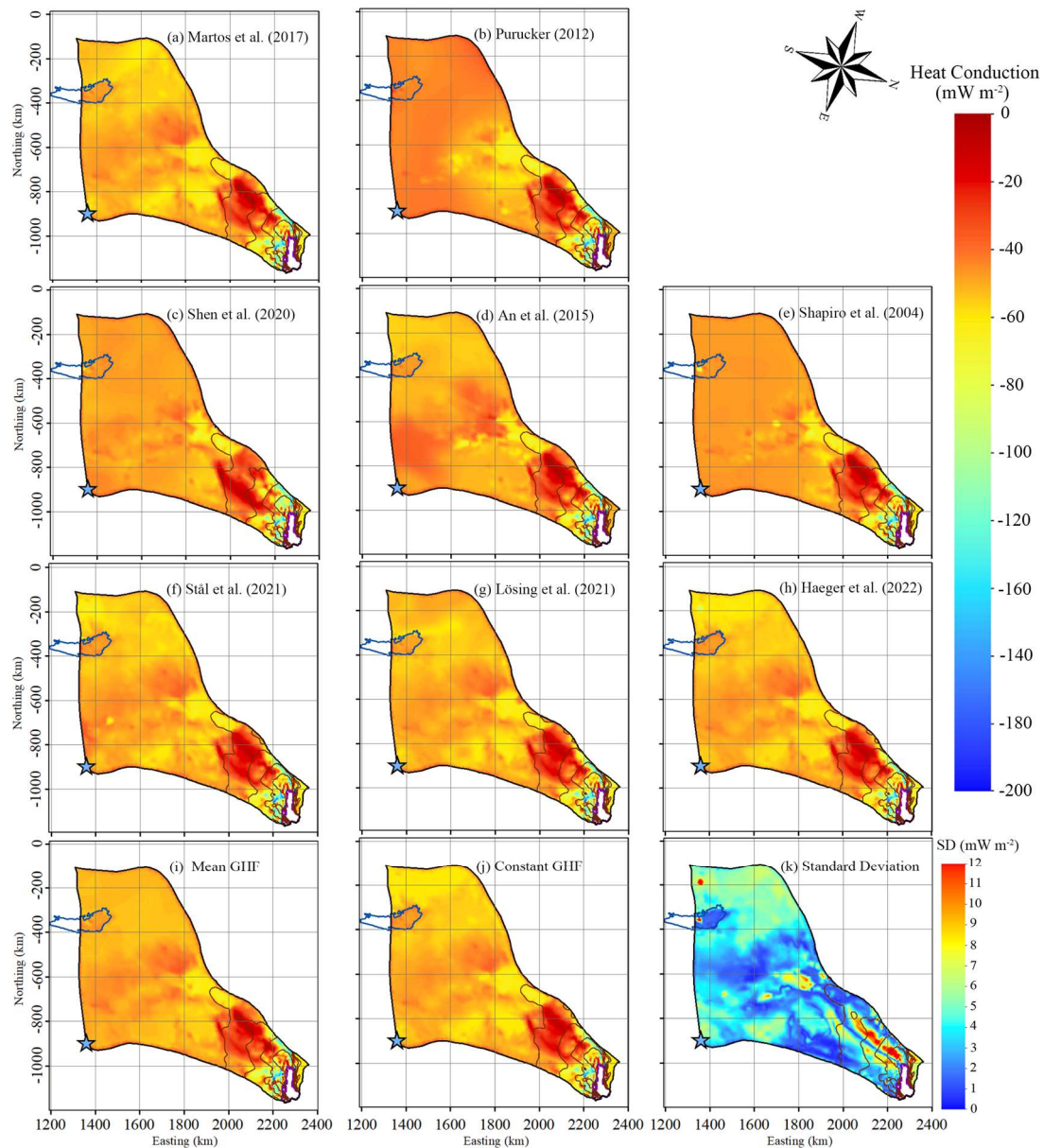
298
 299 The distribution of modeled basal friction heat is closely associated with that of
 300 modelled basal velocity. The patterns of basal friction heat with different GHFs are very
 301 similar in fast flow region, but have some differences in the middle of the domain (Fig.
 302 6) where modelled basal velocity ranges between 5-20 m yr⁻¹ (Fig. 4).

303
 304 The modelled basal friction heat is close to 0 where the surface ice velocity is less than
 305 10 m yr⁻¹, but ranges widely by 10-2000 mW m⁻² elsewhere, with SD between 1 mW m⁻²
 306 and 200 mW m⁻² in the fast flowing region. Basal friction heating larger than 100 mW

307 m^{-2} occurs where surface velocity is more than 50 m yr^{-1} and basal velocity is higher
308 than 10 m yr^{-1} (Fig. 6; Fig. 4), and it is then the dominant heat source.
309



310
311



312

313 Fig. 7. Modelled heat change of basal ice by upward englacial heat conduction. The negative sign
 314 means that the upward englacial heat conduction causes heat loss from the basal ice as defined by
 315 the color bar with cooler colors representing more intense heat loss by conduction. (a) to (e)
 316 corresponding to the GHF (a) to (e) in Fig. 2. **Panel (k) is the standard deviation of 8 modelled basal**
 317 **friction heat (a)-(h).** The **black** solid curves represent modelled surface speed contours of 30,
 318 50, 100 and 200 m yr⁻¹, as in Fig. 44. **The purple line depicts the grounding line. The blue curve**
 319 **depicts Lake Vostok. The blue star denotes Dome C.**

320

321 Fig. 7 shows the modeled heat change of basal ice by upward englacial heat conduction
 322 in the **five** experiments. In the slow-flowing region where basal temperature is below
 323 the pressure melting point, the upward basal heat conduction equals the GHF (Fig. 5,
 324 Fig. 7). In the **fast-flowing** region **where basal temperature reaches pressure melting**
 325 **point (Fig. 5) with low basal velocity (Fig. 4e) and thick ice (≥ 2500 m; Fig. 1c), the**

326 heat loss caused by upward basal heat conduction is $< 30 \text{ mW m}^{-2}$ in all experiments
327 (Fig. 7), reflecting the development of a temperate basal layer that limits the basal
328 thermal gradient. In the fast-flowing tributaries with high basal velocity (Fig. 4e) and
329 ice thickness $< 2000 \text{ m}$, the ~~heat loss caused by combination of reduced ice thickness and~~
330 increased concentration of shear heating at the basal plane rather than in the lower ice
331 column removes the temperate layer and allows very large values of upward basal heat
332 conduction ~~can be very large, 100, up to 60-200~~ mW m^{-2} near the grounding line (Fig.
333 7).

334

335 **4.4 Basal Melt Rate**

336 We calculate basal melt rate using the thermal balance equation (Eq 3). There are
337 significant differences in the fiveten experiments due to large variability in GHF (Fig.
338 8). The Martos et al. ~~(2017)~~(2017), Haeger et al. (2022), Stål et al. (2021), and ~~then~~
339 ShenLösing et al. (2020)2021 GHF yield the largest areas with basal melting. The
340 experiments using Shen et al. (2020), An et al. (2015), Shapiro and Ritzwoller (2004)
341 and Purucker ~~et al. (2013)~~(2012) GHF yield less and similar total basal melting areas
342 but have different spatial patterns. The basal melting area produced by the experiment
343 using ensemble mean GHF is between the four large areas and the four small areas. But
344 the basal melting area produced by the constant GHF is larger than that by all the 8
345 GHF (Fig. 8).

346

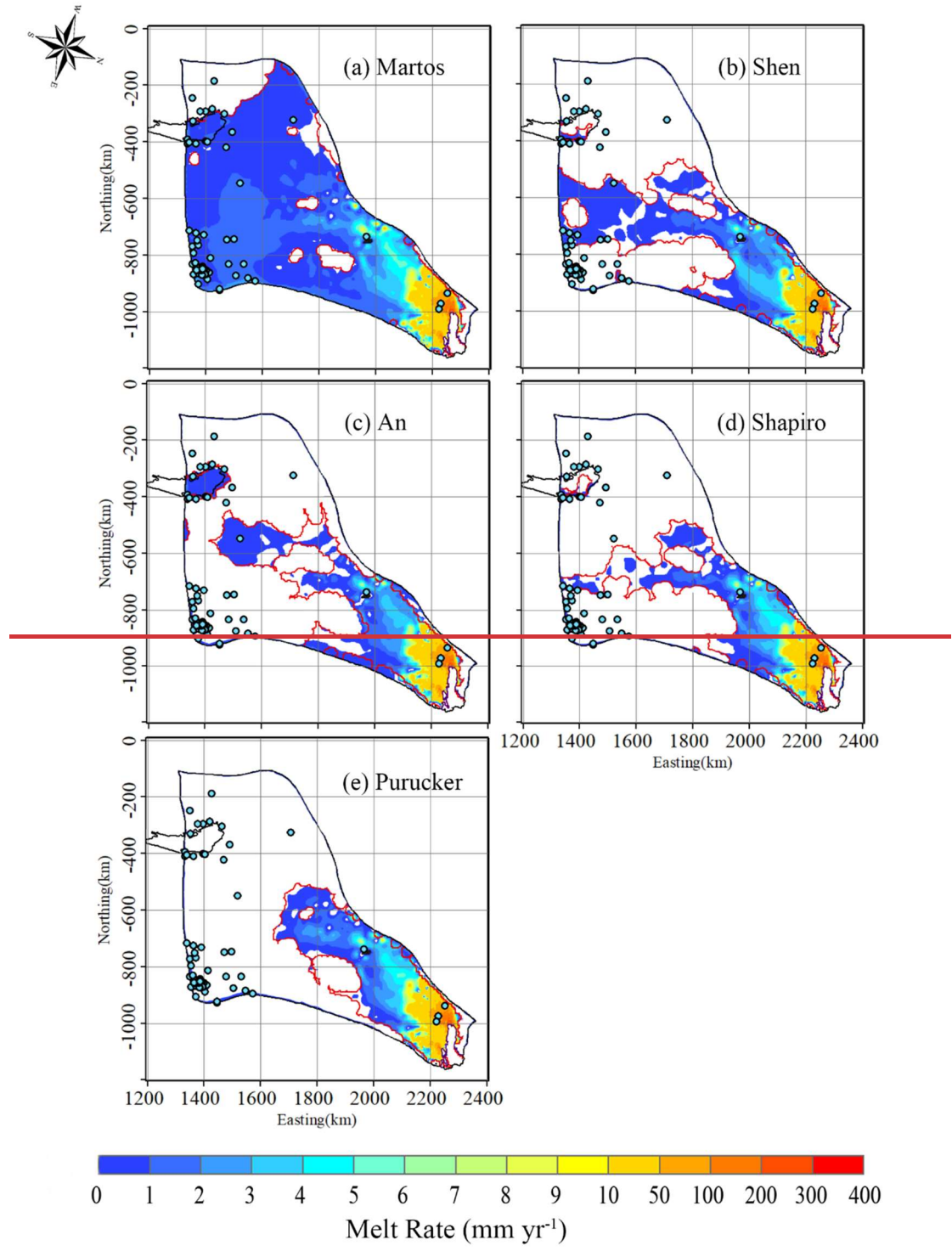
347 In most of the warm based regions, the modeled basal melting rate is $< 5 \text{ mm yr}^{-1}$ (Fig.
348 8) and basal friction heat is $< 50 \text{ mW m}^{-2}$ (Fig. 6). Basal melting rates $> 5 \text{ mm yr}^{-1}$ occur
349 with surface velocities $> 100 \text{ m yr}^{-1}$ (Fig. 4, Fig. 8), where the basal friction heat is the
350 dominant heat source. In particular, the modeled basal melting rate is $50\text{-}400 \text{ mm yr}^{-1}$
351 in the two fast flow tributaries feeding the ice shelf that have surface velocities > 200
352 m yr^{-1} , and where the basal friction heat can reach $500\text{-}2000 \text{ mW m}^{-2}$ (Fig. 4, Fig. 6, Fig.
353 8). This is consistent with the findings of Larour et al. (2012) and Kang et al. (2022),
354 that the slow-flowing ice is more sensitive to GHF while the fast-flowing region is more
355 sensitive to basal friction heat.

356

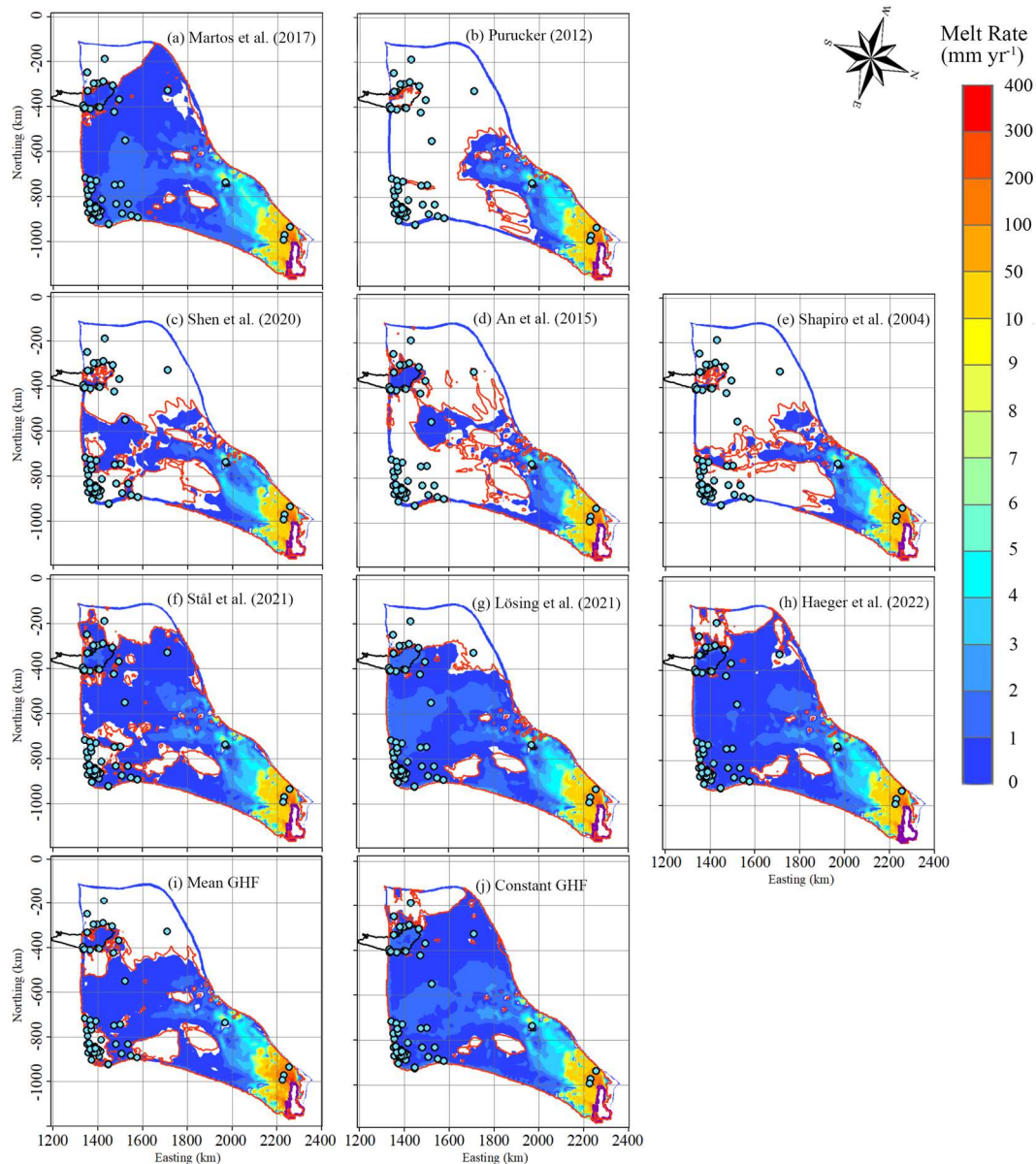
357 There is relatively high modelled basal melt rate ($4\text{-}10 \text{ mm yr}^{-1}$) localized at the central
358 subglacial canyon (Fig. 8, Fig. 1c), which is captured by all fiveten GHF experiments,
359 and also consistent with the high values (0.5-1.0) of specularly content data there (Fig.
360 9). Dow et al. (2020) found that the specularly content is a useful proxy for both water
361 depth and water pressure in regions of distributed water in subglacial canyons.

362

363 There is a location with modelled refreezing (negative melting rate) at the central
364 subglacial canyon, near the observed subglacial lake, in all fiveten GHF experiments
365 (Fig. 8). The value of specularly content there is low as $0\text{-}0.1$ (Fig. 9), and freeze on is
366 driven by the steep topography around the canyon.



367
368



369

370 Fig. 8. Modelled basal melt rate, (a) to (e) correspond to the GHF (a) to (e) in Fig. 2. The ice bottom
 371 at pressure-melting point is surrounded by a red contour. The black curve depicts Lake
 372 Vostok. Stable subglacial lakes are shown as blue-green points with black circles. The purple line
 373 depicts the grounding line. There is modelled basal refreezing at the central canyon painted in black.

374

375 4.5 Evaluation of modelled results with 58 GHFs

376 We use the locations of the observed subglacial lakes and specularity content to
 377 discriminate between modeled basal melting (Fig. 8). Ideally, we would like to have a
 378 modeled ice base that is cold and dry where subglacial lakes do not exist and the
 379 specularity content is low, and a modeled ice base that is at the melting point where
 380 lakes and high specularity content are observed. In other words, we would like to use
 381 the available data to form a two-sided constraint that can penalize the model for being
 382 both too warm and too cold. If we only have a one-sided constraint, then we would

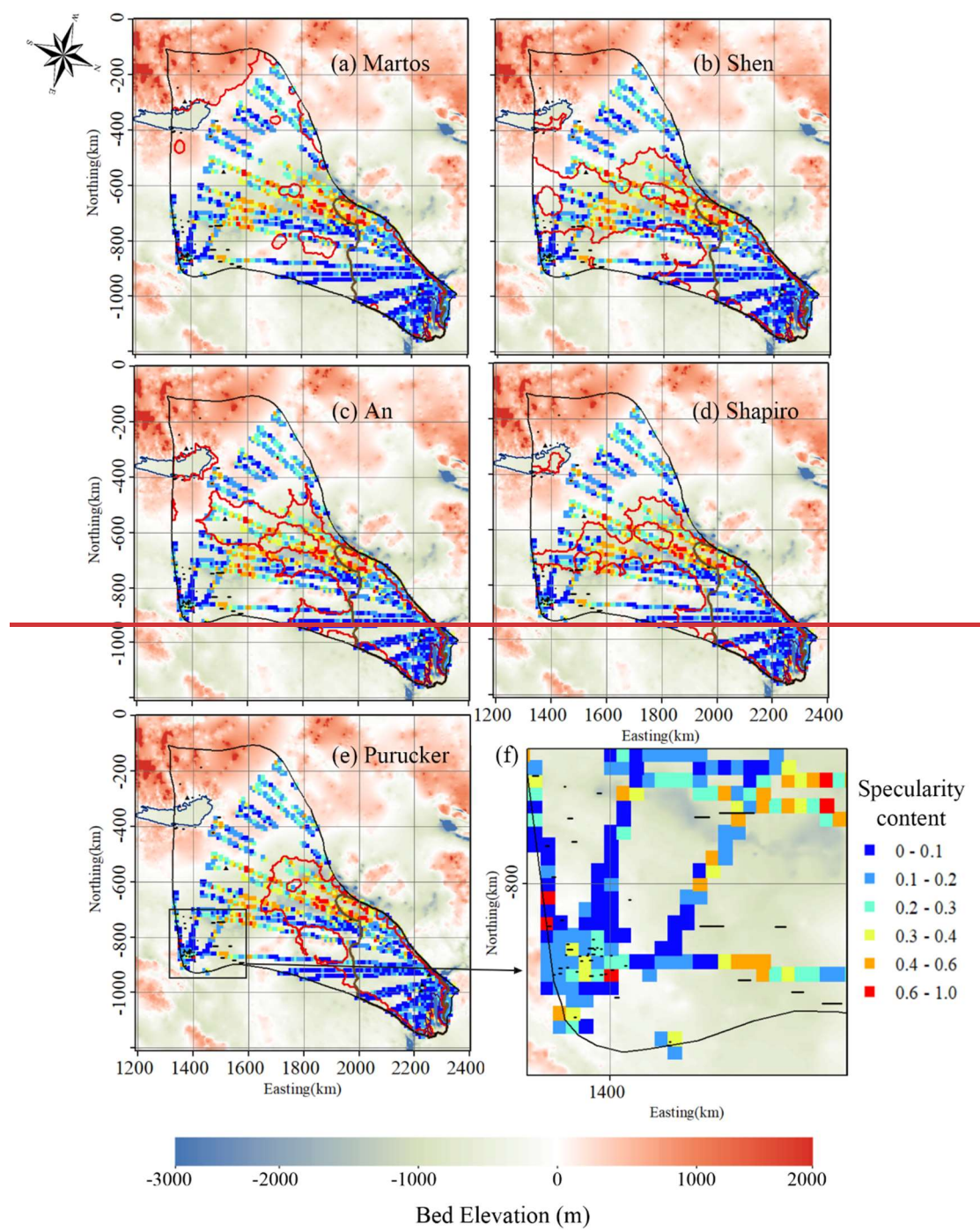
383 always end up concluding that either the warmest or the coldest GHF map is best,
384 regardless of whether that map was a reasonable representation of the basal state.

385

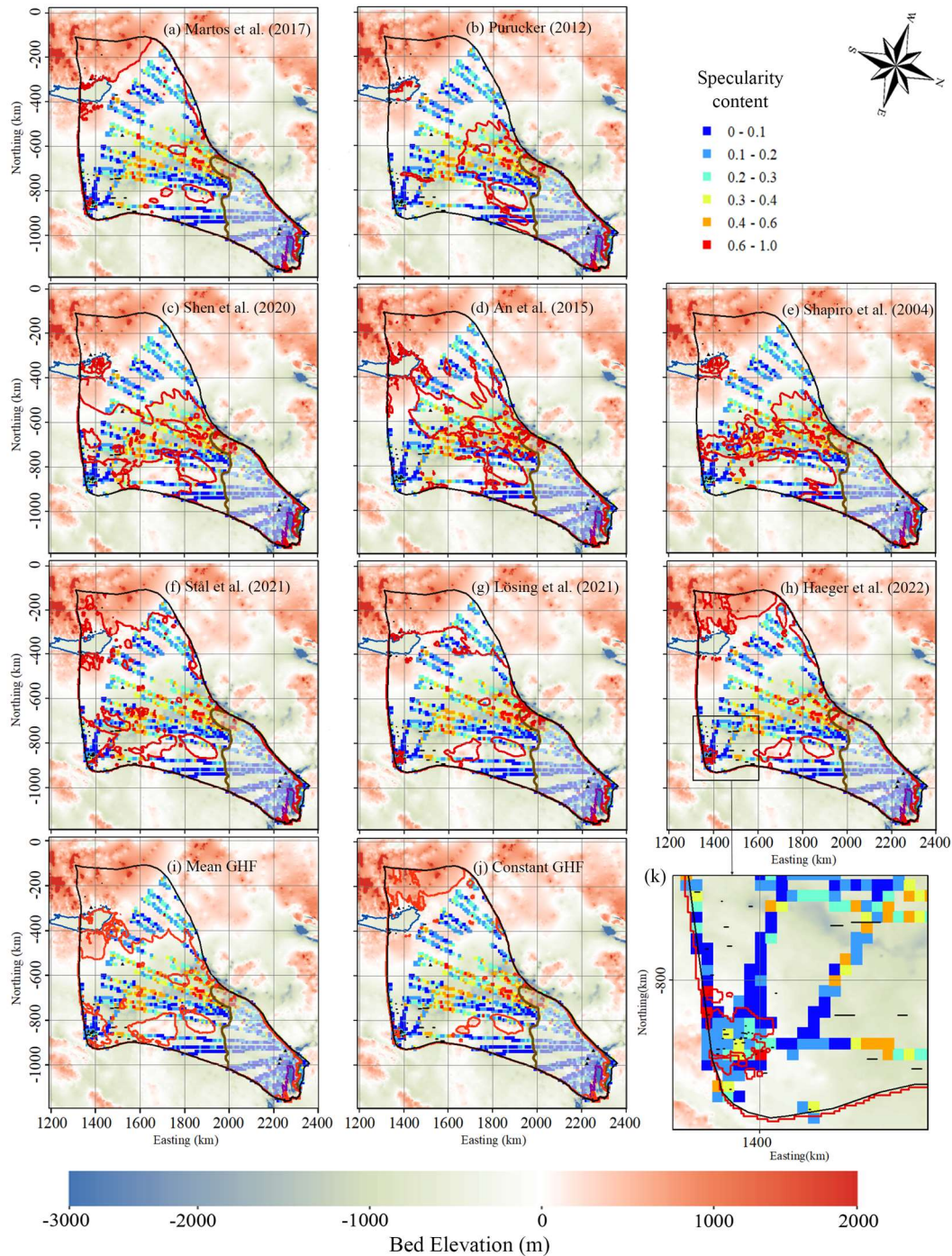
386 Observations of subglacial lakes are mostly a one-sided constraint on the basal thermal
387 state. This is because lakes are only detectable if subglacial water accumulates in
388 depressions that are deep compared to the radar wavelength and wide in comparison to
389 the horizontal resolution of the radar system. Other forms of distributed hydrology,
390 such as linked cavities or saturated subglacial sediments, do not produce the classic flat
391 bright reflectors characteristic of subglacial lakes. Thus, the lack of observed subglacial
392 lakes in a particular region cannot be taken as evidence that there is no subglacial water
393 there. The mesh resolution of our model inland is about 20 km (Fig. 3). But 84% of the
394 subglacial lakes have along-radar track lengths below 5 km, 94% are below 10 km, with
395 only 5 lakes including Lake Vostok above 10 km (Fig. 9f). So the subglacial lakes may
396 be too small for the ice model to resolve. Nonetheless, we compare our modeled basal
397 thermal state with the observed locations of subglacial lakes. These comparisons show
398 that all the experiments can capture all four subglacial lakes in the fast-flowing region
399 (Fig. 8). But their performance in covering subglacial lakes in the slow-flowing region
400 differ greatly.

401

402 In addition to the subglacial lakes, we use specularity content to derive a two-sided
403 constraint on basal thermal state. Specularity content is an inherently noisy measure, so
404 it is smoothed to 1 km along track values, and furthermore it is not unambiguously an
405 indicator of wet beds. For example, specularity content is low in the fast-flowing region
406 (Fig. 9, Fig. 4), where there must be lubricating water at the bed. Similar specularity
407 results were also seen by Schroeder et al. (2013) for Thwaites Glacier, where high
408 specularity values are seen under the major tributaries and the upstream trunk, but
409 significant lower values of specularity in the fast-flowing region. This counter-intuitive
410 result may be due to distinct morphologies and radar scattering signatures between
411 water distributed in widespread subglacial conduits and water concentrated in just a few
412 subglacial channels. Because of this effect, we only use the specularity content outside
413 the fast-flowing region (defined as surface speed $>30 \text{ m a}^{-1}$, Fig. 9).



414
415



416

417 Fig. 9. Locations of specularity content (colored points) derived from radar data collected by
 418 ICECAP (Dow et al., 2020) and interpolated to 10 km by 10 km grids under the background of
 419 bedrock elevation. Specularity content > 0.4 indicates the likely presence of basal water. The ice
 420 bottom at pressure-melting point is surrounded by a red contour, (a) to (e) correspond to the five
 421 GHF maps (a) to (e) in Fig. 2. Lake Vostok is outlined by a blue curve. The brown curve is the
 422 contour of surface speed of 30 m a^{-1} . Subglacial lakes are shown at observed positions as a line
 423 segment of their length. Plot (k) is a zoom of the box in plot (e).

424

425 The specularity content data calculated from ICECAP survey lines suggests hundreds

426 of locations with basal water (Dow et al., 2020). The default resolution of specularity
 427 content along the flight lines is 1 km (Dow et al., 2020), which is smaller than our model
 428 resolution of 6-20 km in the slow flowing region. Water may accumulate in just a small
 429 fraction of the grid cell even if the majority of the cell is warm because of water flow.
 430 For comparability, with our simulation resolution we aggregated the specularity content
 431 data onto 10 km by 10 km windows (Fig. 9). The 10 km window is a somewhat arbitrary
 432 choice, but smaller windows (we tried 2 and 5 km) reduce the data available and noise
 433 becomes larger, while larger windows (we tried 15 and 20 km) restrict spatial resolution.
 434 We then take the upper fifth percentile of the specularity content, *specularity₅* of each
 435 window as a water indicator rather than its mean value to allow for localized water
 436 collection or unfavorable bed reflection geometry, while also excluding spurious signals
 437 in the noisy specularity data. Young et al. (2016) suggested that specularity larger than
 438 0.4 was an indicator of a warm bed. This is also consistent with the largest subglacial
 439 lake in the domain with length of 28 km having specularity content >0.4 (Fig. 9f).
 440 There are also some smaller lakes (several km along-track lengths) with specularity
 441 content between 0.2 and 0.4, so a warm threshold of 0.4 would not capture these
 442 features. The cold threshold need not be the same as the warm bed one, and so we
 443 explored different values for cold thresholds of 0.2, 0.3, 0.4, but found that the 0.2 cold
 444 threshold provided best discrimination between models, and also maximizes the
 445 available data.

446
 447 To evaluate modelled basal conditions with specularity content, we define a warm hit
 448 rate as the ratio of the number of grid cells with modelled warm bed that have
 449 *specularity₅* > 0.4 to the total number of grids with *specularity₅* > 0.4. Similarly, cold
 450 hit rate is defined as the ratio of the number of grid cells with *specularity₅* < 0.2.

451
 452 One simple measure of quality is just the average of warm hit rate and cold hit rate, but
 453 we also want an unbiased evaluation of GHF to have similar capabilities in capturing
 454 both warm bed and cold bed regions. Therefore, we define *imbalance* as

$$455 \quad \textit{imbalance} = \frac{\textit{warm hit rate} - \textit{cold hit rate}}{\textit{warm hit rate} + \textit{cold hit rate}},$$

456 as it reflects the difference between warm hit rate and cold hit rate, and has a value
 457 between -1 and 1. The closer to zero *imbalance* is, the more confidence we have in the
 458 model result. The overall performance is estimated by averaged hit rate minus the
 459 absolute value of *imbalance*.

460
 461 The Martos constant GHF has yields the highest higher warm hit rate and the lower cold
 462 hit rate than any single GHF map since it produces larger warm bed area. The four
 463 highest GHF, Martos et al. (2017), Haeger et al. (2022), Stål et al. (2021), and Lösing
 464 et al. (2021) GHF have similarly the highest warm hit rate and lowest cold hit rate
 465 among the 8 GHF since it has they have the largest modelled warm bed area. The
 466 averaged hit rates of modelled results with 58 GHF are very close, with differences <
 467 0.13 (Table 3). The Shapiro, and Ritzwoller (2004), Purucker, (2012), then Shen et al.
 468 (2020) have the highest averaged hit rate using all the values for threshold of cold bed,

469 and the differences between their averaged hit rate < 0.04 . The mean GHF has the same
 470 averaged hit rate as Shen et al. (2020).

471

472 Martos et al. (2017), Haeger et al. (2022), Stål et al. (2021), and Shen-Lösing et al.
 473 (2021) GHF have large positive imbalance > 0.5 , which means that their warm hit rate
 474 is higher than rates overwhelm their cold hit rates. Shen et al. rate. (2020) has positive
 475 but near-zero imbalance.

476 In contrast, An et al. (2015), Shapiro and Ritzwoller (2004) and Purucker (2012) GHF
 477 have negative imbalance. ~~Martos has the largest imbalance because its warm hit rate~~
 478 ~~overwhelms its cold hit rate. The absolute imbalance of Shen is < 0.05 with all three~~
 479 ~~cold hit thresholds we used and always the smallest (Table 3) of the GHF. The Shapiro~~
 480 ~~absolute imbalance the second smallest with all the cold hit thresholds. Therefore, Shen~~
 481 ~~and Shapiro rank the top two according to imbalance between warm hit rate and cold~~
 482 ~~hit rate.).~~

483

484 Considering the overall performance by averaged hit rate minus the absolute value of
 485 imbalance, Shen et al. (2020) ranks the best first, Shapiro and Ritzwoller (2004) the
 486 second, Purucker (2012) the third, An et al. (2015) the fourth and, Martos et al. (2017),
 487 Stål et al. (2021), Lösing et al. (2021) and Haeger et al. (2022) get negative score, and
 488 rank the last four among the 8 GHF (Table 3). The ensemble mean GHF gets score close
 489 to An et al. (2015). The constant GHF gets lower score than any GHF. The ranking is
 490 robust with all three cold hit thresholds.

491

492 Table 3. Warm hit rate, cold hit rate, averaged hit rate, imbalance and overall
 493 performance for the modelled results with 5 GHFs, eight individual GHF maps,
 494 ensemble mean GHF, and constant GHF of 58.75 mW m^{-2} in Table 2. The overall
 495 performance is calculated by averaged hit rate minus the absolute value of imbalance.
 496 The threshold of *specularity*₅ is taken as 0.4 for warm hit rate, and 0.2 for cold hit rate.

GHF	warm hit rate	cold hit rate	averaged hit rate	Imbalance	<u>averaged hit rate - abs(imbalance) over all performance</u>
Martos et al., 2017	0.9560	0.1648	0.56	0.71	-0.15
Purucker, 2012	<u>0.5283</u>	<u>0.8201</u>	<u>0.67</u>	<u>-0.22</u>	<u>0.45</u>
Shen et al., 2020	0.6588	0.6564	0.65	0.0018	0.65
An et al., 2015	0.4340	0.7652	0.60	-0.28	0.32
Shapiro and Ritzwoller, 2004	0.5975	0.7822	0.69	-0.13	0.56
Purucker Stål et al., 2021	<u>0.5283875</u> <u>0</u>	<u>0.820124</u> <u>05</u>	<u>0.6756</u>	<u>-0.2257</u>	<u>-0.4501</u>
Lösing et al., 2021	<u>0.9313</u>	<u>0.2216</u>	<u>0.58</u>	<u>0.62</u>	<u>-0.04</u>
Haeger et al., 2022	<u>0.9688</u>	<u>0.1458</u>	<u>0.56</u>	<u>0.74</u>	<u>-0.18</u>
Mean GHF	<u>0.8750</u>	<u>0.4205</u>	<u>0.65</u>	<u>0.35</u>	<u>0.30</u>

<u>Constant GHF</u>	<u>0.9813</u>	<u>0.1042</u>	<u>0.54</u>	<u>0.81</u>	<u>-0.27</u>
---------------------	---------------	---------------	-------------	-------------	--------------

497

498 **5 Discussion**

499 Wright et al. (2012) modelled basal temperature of Totten Glacier using the Glimmer
500 ice sheet model with a constant GHF of 54 mW m^{-2} . Their modelled area of basal warm
501 ice is between what we simulated using Martos et al. (2017) and Shen et al. (2020),
502 GHF, covering most of the lakes and lake-like features but missing some near Lake
503 Vostok. Dow et al. (2020) ran the Ice Sheet System Model (Larour et al., 2012) with a
504 constant GHF of 55 mW m^{-2} , producing a warm bed region slightly larger than we
505 simulated using the Shen et al. (2020) GHF (which has a mean of 58 mW m^{-2} in this
506 region, Table 2). ~~Eisen et al. (2020) modeled the basal temperature of Antarctic ice sheet
507 with the Parallel Ice Sheet Model using four different GHF datasets (Shapiro and
508 Ritzwoller, 2004; Fox Maule et al., 2005; An et al., 2015; Martos et al., 2017). The
509 mean modelled basal temperature of the different GHFs appear close to our result using
510 the However, our experiment with a constant GHF of 59 mW m^{-2} produces warm bed
511 region almost as large as that with Martos et al. (2017) GHF suggesting this constant
512 value is too high for this domain. Our experiment with ensemble mean GHF gives warm
513 bed region close to that by Shen et al. (2020) GHF, indicating ensemble mean is a better
514 choice than the mean of ensemble mean Shen et al. (2020) GHF, with basal temperatures
515 reaching the pressure melting point in the fast flow region and the central upstream
516 region of Totten Glacier.~~

517

518 Kang et al. (2020) evaluated basal thermal conditions underneath the Lambert-Amery
519 glacier system using six GHFs, and found that the two most recent GHF fields inverted
520 from aerial geomagnetic observations and which have the highest GHF values,
521 produced the largest warm-based area, and best matched the observed distribution of
522 subglacial lakes. This might be expected as there was only a one-sided constraint used,
523 and warm based models produced matches with more lakes.

524

525 Although the basal ice in fast-flowing regions is all at pressure melting point because
526 basal friction heat dominates the heat balance, the modelled basal melt rate of the
527 grounded ice in fast-flowing regions exhibits large differences across-models. The
528 modelled basal melt rate is associated with the modelled basal friction heat, which is a
529 function of the modelled basal velocity and basal shear stress, the accuracy of which
530 depends on the configuration and constraints of the ice sheet model used. Our modelled
531 maximum basal melt rate on the grounded ice is 0.4 m yr^{-1} near the grounding line. This
532 is close to the modelled maximum basal melt rate of 0.34 m yr^{-1} near the grounding line
533 by Dow et al. (2020), where they calculated the basal melt rates as a function of
534 combined GHF and frictional heating using the Ice Sheet System Model. We know of
535 no observations of the basal melt rates of grounded ice in Totten Glacier.

536

537 Modelled basal sliding speeds by Dow et al. (2020) range from 0.06 m yr^{-1} inland to
538 900 m yr^{-1} at the grounding line, which is close to our result (Fig. 4). Dow et al (2020)
539 simulate basal sliding generally where bedrock is below sea level, with an area close to

540 our simulation with a basal sliding coefficient β_{old} and which is larger than ours using
541 the improved basal sliding coefficient β_{new} (Eq 2) found by considering the basal
542 temperature relative to pressure-melting point. The modelled basal sliding speed
543 reaches a local maximum at the middle of the subglacial canyon system (Fig. 4), which
544 leads to local maxima in basal friction and basal melt rate (Fig. 8), and is consistent
545 with the high values of specularity (Fig. 9).

546

547 To evaluate the simulation results, we compare the simulated basal melting area with
548 the locations of the discovered subglacial lakes and specularity content derived from
549 radar data collected by ICECAP (Dow et al., 2020). Specularity is a parameterization
550 that estimates the along-track angularly narrow component of bed echo energy
551 compared with the isotropic diffuse energy component (Schroeder et al., 2015).
552 Specularity is determined by a set of ice/bed properties including the length, width and
553 thickness of the water body, its conductivity, and the roughness of the ice/water
554 interface. Off-nadir across-track reflectors may also produce glints creating noise in the
555 specularity distribution. Hence, interpretation of specularity is ambiguous and
556 dependent on the local bed morphology. This led us to experiment with a range of
557 windows over which to aggregate the bed reflection energy, and various thresholds for
558 estimating cold and warm beds. We were able to use the numerous subglacial lakes in
559 the region as a guide to setting these parameters, bearing in mind that the observations
560 of subglacial lakes are a one-sided constraint. If the modeled basal melting area misses
561 the subglacial lake or high specularity content, the model is underestimating the basal
562 temperature at that location. However, if the basal melting is simulated in areas without
563 observed subglacial lakes, it is unclear if this is because the models overestimate the
564 temperature in those areas, or if the water under the ice sheet has not been detected.

565 ~~Moreover, a hypersaline lake and various other water saturated environments seem to~~
566 ~~exist below cold ice beneath Devon Island ice cap in Canada (Rutishauser et al., 2022).~~

567 In addition, relatively high electrical conductivity beds like water saturated clays can
568 lead to false positives in radar detections of subglacial water bodies (Talalay et al.,
569 2020).

570

571 Our evaluation using specularity content is a two-sided constraint and thus improves on
572 observed subglacial lakes as a discriminating feature of cold and warm beds. ~~The~~
573 ~~experiment with~~ Using subglacial lakes as a one-sided constraint, Haeger et al., (2022)
574 and Martos et al. (2017) GHF models rank the top two as they model the largest region
575 of basal melt, ~~and covers most observed subglacial lake locations. However, it~~ however,
576 they ranks ~~worst in the evaluation~~ last two using specularity content; as a two-sided
577 constraint because it cannot capture cold beds well.

578

579 **6 Conclusions**

580 In this study we diagnose the basal thermal state of Totten Glacier by coupling a forward
581 model and an inverse model and using fiveeight different GHFs. By comparing
582 modelled basal temperature distributions with metrics derived from specularity content
583 data we evaluate the reliability of the fiveeight GHF data in this area.

584

585 We find there are significant differences in the spatial distributions of modelled
586 temperate ice with different GHFs, and the differences are mainly concentrated in the
587 slow ice flow regions. The modelled basal thermal state (frozen/melting) in the slow
588 ice flow region is mainly determined by the heat balance between GHF and englacial
589 upward heat conduction, and the basal melting rate is generally less than 5 mm yr⁻¹.
590 However, there is local maximum in modelled basal melt rate (4-10 mm yr⁻¹) at the
591 central subglacial canyon, which could be explained by the local high basal sliding
592 velocity and frictional heat that are captured by all GHF experiments. This is consistent
593 with the high values of specularly content data there.

594

595 The basal heat balance in the fast ice flow region is mainly determined by the basal
596 frictional heat. The basal ice in the fast flow region is all at the melt point. The modeled
597 basal melting rate is 50-400 mm yr⁻¹ in the two fast flow tributaries feeding the ice shelf
598 with surface velocity greater than 200 m yr⁻¹, where the basal friction heat is 500-2000
599 mW m⁻².

600

601 Our evaluation using specularly content as a two-sided constraint, gives quite different
602 result than only using observed locations of subglacial lakes. Simulations with the
603 Martos et al. (2017), Haeger et al., (2022), Stål et al. (2021), and Lösing et al. (2021)
604 GHF ~~yields~~ the largest region of basal melt, which covers most observed
605 subglacial lake locations, however, ~~itstheir~~ cold bed fit with specularly content is poor
606 and shows huge imbalance in modelling warm bed and cold bed regions. Overall,
607 Martos et al. (2017), Haeger et al., (2022), Stål et al. (2021), and Lösing et al. (2021)
608 GHF ~~ranks~~ last in the evaluation with specularly content. The constant GHF, area
609 average of ensemble mean of the eight GHF produces a lower score than any of the
610 eight individual GHF maps. The ensemble mean GHF gets the middle ranks. Shen et al.
611 (2020) GHF yields the second largest area of basal melt and second best agreement with
612 the locations of the subglacial lakes, and also scores well in modelling both warm and
613 cold bed areas. -Shen et al. (2020) GHF and Shapiro and Ritzwoller (2004) GHF rank
614 the top two according to the evaluation with specularly content. The best-fit simulated
615 result shows that most of the inland bed area is frozen. Only the upstream subglacial
616 canyon inland reaches pressure-melting point, and modelled basal melting rate there is
617 0-10 mm yr⁻¹.

618

619 **Data availability**

620 MEaSURES BedMachine Antarctica, version 2, is available at
621 <https://doi.org/10.5067/E1QL9HFQ7A8M> (Morlighem, 2020). MEaSURES InSAR-
622 based Antarctic ice velocity Map, version 2, is available at
623 <https://doi.org/10.5067/D7GK8F5J8M8R> (Rignot et al., 2017). MEaSURES Antarctic
624 Boundaries for IPY 2007–2009 from Satellite Radar, version 2 is available at
625 <https://doi.org/10.5067/AXE4121732AD> (Mouginot et al., 2017). The subglacial lake
626 dataset is available at <https://doi.org/10.1038/s43017-021-00246-9> (Livingstone et al.,
627 2022). The specularly content dataset <https://doi.org/10.5281/zenodo.3525474> (Dow

628 et al., 2020). ALBMAP v1 and the GHF dataset of Shapiro and Ritzwoller (2004) are
629 available at <https://doi.org/10.1594/PANGAEA.734145> (LeBrocq et al.,
630 2010b). The GHF dataset of An et al. (2015) is available at
631 <http://www.seismolab.org/model/antarctica/lithosphere/AN1-HF.tar.gz> (last access: 11
632 April 2023). The GHF dataset of Shen et al. (2020) is available at
633 <https://sites.google.com/view/weisen/research-products?authuser=0> (last access: 11
634 April 2023). The GHF dataset of Martos (2017) is available at
635 <https://doi.org/10.1594/PANGAEA.882503>. The GHF dataset of Purucker (2012) is
636 available at http://websrv.cs.umt.edu/isis/index.php/Antarctica_Basal_Heat_Flux (last
637 access: 11 April 2023). The modelled basal temperature, basal melt rate and the upper
638 fifth percentile of the specularity content in this paper will be available at
639 <https://doi.org/10.5281/zenodo.7825456>.

640

641 **Author contributions.**

642 LZ and JCM conceived the study. LZ, MW, and JCM designed the methodology. YH,
643 LZ, and YM carried out the simulations and produced the estimates and figures. LZ
644 wrote the original draft, and all the authors revised the paper.

645

646 **Competing interests.**

647 The authors declare no conflict of interest.

648

649 **Acknowledgments**

650 This work was supported by ~~the National Natural Science Foundation of China (No.~~
651 ~~41941006)~~, National Key Research and Development Program of China
652 (2021YFB3900105), ~~the National Natural Science Foundation of China (No.~~
653 ~~41941006)~~, State Key Laboratory of Earth Surface Processes and Resource Ecology
654 (2022-ZD-05) and Finnish Academy COLD Consortium (No. 322430).

655

656 **References**

657 Adusumilli, S., Fricker, H. A., Medley, B., Padman, L., and Siegfried, M. R.:
658 Interannual variations in meltwater input to the Southern Ocean from Antarctic ice
659 shelves, *Nat. Geosci.*, 13, 616–620, <https://doi.org/10.1038/s41561-020-0616-z>,
660 2020.

661 An, M., Wiens, D. A., Zhao, Y., Feng, M., Nyblade, A., Kanao, M., Li, Y., Maggi, A.,
662 and L ev eque, J.: Temperature, lithosphere-asthenosphere boundary, and heat flux
663 beneath the Antarctic Plate inferred from seismic velocities, *J. Geophys. Res.-Solid*
664 *Earth,-Sol. Ea.*, 120, ~~8720–8742~~359–383, <https://doi.org/10.1002/2015JB011917>,
665 2015.

666 Bell, R. E., Studinger, M., Shuman, C. A., Fahnestock, M. A., and Joughin, I.: Large
667 subglacial lakes in East Antarctica at the onset of fast-flowing ice streams, *Nature*,
668 445, 904–907, <https://doi.org/10.1038/nature05554>, 2007.

669 ~~Chen, J. L., Wilson, C. R., Blankenship, D., and Tapley, B. D.: Accelerated Antarctic~~
670 ~~ice loss from satellite gravity measurements, *Nature Geosci.*, 2, 859–862,~~
671 ~~<https://doi.org/10.1038/ngeo694>, 2009.~~

672 [Bullard, E. C.: The disturbance of the temperature gradient in the earth's crust by](#)
673 [inequalities of height, *Geophysical Supplements, Mon. Not. R. Astron. Soc.*, 4,](#)
674 [360–362, <https://doi.org/10.1111/j.1365-246X.1938.tb01760.x>, 1938.](#)

675 [Colgan, W., MacGregor, J. A., Mankoff, K. D., Haagenson, R., Rajaram, H., Martos, Y.](#)
676 [M., Morlighem, M., Fahnestock, M. A., and Kjeldsen, K. K.: Topographic](#)
677 [correction of geothermal heat flux in Greenland and Antarctica, *J. Geophys. Res.-*](#)
678 [Earth, 126, e2020JF005598, <https://doi.org/10.1029/2020JF005598>, 2021.](#)

679 Comiso, J. C.: Variability and Trends in Antarctic Surface Temperatures from In Situ
680 and Satellite Infrared Measurements, *J. Climate*, 13, 1674–1696,
681 [https://doi.org/10.1175/1520-0442\(2000\)013<1674:VATIAS>2.0.CO;2](https://doi.org/10.1175/1520-0442(2000)013<1674:VATIAS>2.0.CO;2), 2000.

682 ~~[Cuffey, K. M., and Paterson, W. S. B.: *The physics of glaciers*, fourth edition, Elsevier,](#)~~
683 ~~[Burlington, 2010.](#)~~

684 Dow, C. F., McCormack, F. S., Young, D. A., Greenbaum, J. S., Roberts, J. L., and
685 Blankenship, D. D.: Totten Glacier subglacial hydrology determined from
686 geophysics and modeling, *Earth and Planetary Science Letters, Planet. Sc. Lett.*,
687 531, 115961, <https://doi.org/10.1016/j.epsl.2019.115961>, 2020.

688 Dow, Christine. Aurora Subglacial Basin GlADs inputs, outputs and geophysical data
689 [data set]. Zenodo. <https://doi.org/10.5281/zenodo.3525474>, 2019.

690 ~~[Eisen, O., Winter, A., Steinhage, D., Kleiner, T., and Humbert, A.: Basal roughness of](#)~~
691 ~~[the East Antarctic Ice Sheet in relation to flow speed and basal thermal state, *Ann.*](#)~~
692 ~~[Glaciol., 61, 162–175, <https://doi.org/10.1017/aog.2020.47>, 2020.](#)~~

693 [Fox Maule, C., Purucker, M. E., Olsen, N., and Mosegaard, K.: Heat flux anomalies in](#)
694 [Antarctica revealed by satellite magnetic data, *Science*, 309, 464–467,](#)
695 <https://doi.org/10.1126/science.1106888>, 2005.

696 Fricker, H. A., Siegfried, M. R., Carter, S. P., and Scambos, T. A.: A decade of progress
697 in observing and modelling Antarctic subglacial water systems, *Phil. Trans. R. Soc.*
698 *A.*, 374, 20140294, <https://doi.org/10.1098/rsta.2014.0294>, 2016.

699 Gagliardini, O., Zwinger, T., Gillet-Chaulet, F., Durand, G., Favier, L., de Fleurian, B.,
700 Greve, R., Malinen, M., Martín, C., Råback, P., Ruokolainen, J., Sacchettini, M.,
701 Schäfer, M., Seddik, H., and Thies, J.: Capabilities and performance of Elmer/Ice,
702 a new-generation ice sheet model, *Geosci. Model Dev.*, 6, 1299–1318,
703 <https://doi.org/10.5194/gmd-6-1299-2013>, 2013.

704 Geuzaine, C. and Remacle, J.-F.: Gmsh: A 3-D finite element mesh generator with built-
705 in pre- and post-processing facilities: ~~THE GMSH PAPER~~, *Int. J. Numer. Meth.*
706 ~~*EngngEng.*~~, 79, 1309–1331, <https://doi.org/10.1002/nme.2579>, 2009.

707 Gillet-Chaulet, F., Gagliardini, O., Seddik, H., Nodet, M., Durand, G., Ritz, C., Zwinger,
708 T., Greve, R., and Vaughan, D. G.: Greenland ice sheet contribution to sea-level
709 rise from a new-generation ice-sheet model, *The Cryosphere*, 6, 1561–1576,
710 <https://doi.org/10.5194/tc-6-1561-2012>, 2012.

711 Greve, R., and Blatter, H.: Dynamics of Ice Sheets and Glaciers, [Advances in](#)
712 [Geophysical and Environmental Mechanics and Mathematics, Series Editor:](#)
713 [Hutter, K., Springer, ISBN 978-3-642-03414-5, 2009.](#)

714 ~~[Gudlaugsson, E., Humbert, A., Andreassen, K., Clason, C. C., Kleiner, T., and Beyer,](#)~~
715 ~~[S.: Eurasian ice sheet dynamics and sensitivity to subglacial hydrology, *J. Glaciol.*,](#)~~

716 [63, 556–564, https://doi.org/10.1017/jog.2017.21](https://doi.org/10.1017/jog.2017.21), 2017.

717 ~~Hansen, I. and Greve, R.: Polythermal modelling of steady states of the Antarctic ice~~
718 ~~sheet in comparison with the real world, n.d.~~

719 ~~Haeger, C., Petrunin, A. G., and Kaban, M. K.: Geothermal heat flow and thermal~~
720 ~~structure of the Antarctic lithosphere, *Geochemistry, Geophysics, Geosystems*, 23,~~
721 ~~e2022GC010501, <https://doi.org/10.1029/2022GC010501>, 2022.~~

722 ~~Huybrechts, P.: A 3-D model for the Antarctic ice sheet: a sensitivity study on the~~
723 ~~glacial-interglacial contrast, *Climate Dynamics*, 5, 79–92,~~
724 ~~<https://doi.org/10.1007/BF00207423>, 1990.~~

725 Kang, H., Zhao, L., Wolovick, M., and Moore, J. C.: Evaluation of six geothermal heat
726 flux maps for the Antarctic Lambert–Amery glacial system, *The Cryosphere*, 16,
727 3619–3633, <https://doi.org/10.5194/tc-16-3619-2022>, 2022.

728 ~~Larour, E., Seroussi, H., Morlighem, M., and Rignot, E.: Continental scale, high order,~~
729 ~~high spatial resolution, ice sheet modeling using the Ice Sheet System Model~~
730 ~~(ISSM): ICE SHEET SYSTEM MODEL, *J. Geophys. Res.*, 117, n/a–n/a,~~
731 ~~<https://doi.org/10.1029/2011JF002140>, 2012a.~~

732 ~~Larour, E., Morlighem, M., Seroussi, H., Schiermeier, J., and Rignot, E.: Ice flow~~
733 ~~sensitivity to geothermal heat flux of Pine Island Glacier, Antarctica: ICE FLOW~~
734 ~~SENSITIVITY TO GEOTHERMAL HEAT, *J. Geophys. Res.-Earth*, 117, n/a–~~
735 ~~n/aF04023, <https://doi.org/10.1029/2012JF002371>, 2012b~~2012jf002371, 2012.

736 Le Brocq, A. M., Payne, A. J., and Vieli, A.: An improved Antarctic dataset for high
737 resolution numerical ice sheet models (ALBMAP v1), *Earth Syst. Sci. Data*, 2,
738 247–260, <https://doi.org/10.5194/essd-2-247-2010>, 2010a.

739 ~~Le Brocq, A. M., Ross, N., Griggs, J. A., Bingham, R. G., Corr, H. F. J., Ferraccioli, F.,~~
740 ~~Jenkins, A., Jordan, T. A., Payne, A. J., Rippin, D. M., and Siegert, M. J.:~~
741 ~~Evidence from ice shelves for channelized meltwater flow beneath the Vieli, A.:~~
742 ~~Antarctic Ice Sheet, *Nature Geosci.*, 6, 945–948, dataset in NetCDF format,~~
743 ~~PANGAEA [data set], <https://doi.org/10.1038/ngeo1977>,~~
744 ~~20131594/PANGAEA.734145, 2010b.~~

745 Li, X., Rignot, E., Mouginot, J., and Scheuchl, B.: Ice flow dynamics and mass loss of
746 Totten Glacier, East Antarctica, from 1989 to 2015: ~~TOTTEN GLACIER:~~
747 ~~VELOCITY AND MASS CHANGE~~, *Geophys. Res. Lett.*, 43, 6366–6373,
748 <https://doi.org/10.1002/2016GL069173>, 2016.

749 Livingstone, S. J., Utting, D. J., Ruffell, A., Clark, C. D., Pawley, S., Atkinson, N., and
750 Fowler, A. C.: Discovery of relict subglacial lakes and their geometry and
751 mechanism of drainage, *Nat Commun*, 7, ncomms11767,
752 <https://doi.org/10.1038/ncomms11767>, 2016.

753 Livingstone, S. J., Li, Y., Rutishauser, A., Sanderson, R. J., Winter, K., Mikucki, J. A.,
754 Björnsson, H., Bowling, J. S., Chu, W., Dow, C. F., Fricker, H. A., McMillan, M.,
755 Ng, F. S. L., Ross, N., Siegert, M. J., Siegfried, M., and Sole, A. J.: Subglacial
756 lakes and their changing role in a warming climate, *Nat Rev Earth Environ*, 3,
757 106–124, <https://doi.org/10.1038/s43017-021-00246-9>, 2022.

758 ~~Lösing, M., and Ebbing, J.: Predicting geothermal heat flow in Antarctica with a~~
759 ~~machine learning approach, *J. Geophys. Res.-Earth*, 126, e2020JB021499,~~

760 <https://doi.org/10.1029/2020JB021499>, 2021.

761 [Martos, Y. M.: Antarctic geothermal heat flux distribution and estimated Curie Depths,](#)
762 [links to gridded files, PANGAEA \[data set\],](#)
763 <https://doi.org/10.1594/PANGAEA.882503>, 2017.

764 Martos, Y. M., Catalán, M., Jordan, T. A., Golynsky, A., Golynsky, D., Eagles, G., and
765 Vaughan, D. G.: Heat Flux Distribution of Antarctica Unveiled, *Geophys. Res.*
766 *Lett.*, 44, 11,417-11,426, <https://doi.org/10.1002/2017GL075609>, 2017.

767 ~~Maule, C. F., Purucker, M. E., Olsen, N., and Mosegaard, K.: Heat Flux Anomalies~~
768 ~~in Morlighem, M.: MEaSURES BedMachine Antarctica Revealed by Satellite~~
769 ~~Magnetic, Version 2, Boulder, Colorado USA, NASA National Snow and Ice Data,~~
770 ~~Science, 309, 464–467, Center Distributed Active Archive Center [data set],~~
771 ~~<https://doi.org/10.1126/science.1106888.20055067/E1QL9HFQ7A8M>, 2020.~~

772 ~~Morlighem, M., Rignot, E., Seroussi, H., Larour, E., Ben Dhia, H., and Aubry, D.:~~
773 ~~Spatial patterns of basal drag inferred using control methods from a full Stokes~~
774 ~~and simpler models for Pine Island Glacier, West Antarctica: SPATIAL~~
775 ~~PATTERNS OF BASAL DRAG, *Geophys. Res. Lett.*, 37, n/a–n/a,~~
776 ~~<https://doi.org/10.1029/2010GL043853>, 2010.~~

777 ~~Morlighem, M., Rignot, E., Binder, T., Blankenship, D., Drews, R., Eagles, G., Eisen,~~
778 ~~O., Ferraccioli, F., Forsberg, R., Fretwell, P., Goel, V., Greenbaum, J. S.,~~
779 ~~Gudmundsson, H., Guo, J., Helm, V., Hofstede, C., Howat, I., Humbert, A., Jokat,~~
780 ~~W., Karlsson, N. B., Lee, W., Matsuoka, K., Millan, R., Mouginot, J., Paden, J.,~~
781 ~~Pattyn, F., Roberts, J., Rosier, S., Ruppel, A., Seroussi, H., Smith, E. C., Steinhage,~~
782 ~~D., Sun, B., Van den Broeke, M. R., Van Ommen, T. D., Van Wesse, M., and~~
783 ~~Young D. A.: Deep glacial troughs and stabilizing ridges unveiled beneath the~~
784 ~~margins of the Antarctic ice sheet, *Nat. Geosci.*, 13, 132–137,~~
785 ~~<https://doi.org/10.1038/s41561-019-0510-8>, 2020.~~

786 Mouginot, J., Scheuchl, B., and Rignot, E.: MEaSURES Antarctic Boundaries for IPY
787 2007-2009 from Satellite Radar, Version 2, National Snow and Ice Data Center,
788 ~~10, [data set], <https://doi.org/doi.org/10.5067/AXE4121732AD>, 2017.~~

789 Pattyn, F.: Antarctic subglacial conditions inferred from a hybrid ice sheet/ice stream
790 model, ~~*Earth and Planetary Science Letters*, *Planet. Sc. Lett.*~~, 295, 451–461,
791 <https://doi.org/10.1016/j.epsl.2010.04.025>, 2010.

792 ~~Pittard, M.-L., Roberts, J.-L., Galton-Fenzi, B.-K., and Watson, C.-S.:~~ Sensitivity of the
793 Lambert-Amery glacial system to geothermal heat flux, *Ann. Glaciol.*, 57, 56–68,
794 <https://doi.org/10.1017/aog.2016.26>, 2016.

795 Pollack, H. N., Hurter, S. J., and Johnson, J. R.: Heat flow from the Earth's interior:
796 Analysis of the global data set, *Rev. Geophys.*, 31, 267,
797 <https://doi.org/10.1029/93RG01249>, 1993.

798 Pritchard, H. D., Arthern, R. J., Vaughan, D. G., and Edwards, L. A.: Extensive dynamic
799 thinning on the margins of the Greenland and Antarctic ice sheets, *Nature*, 461,
800 971–975, <https://doi.org/10.1038/nature08471>, 2009.

801 Purucker, M.: Geothermal heat flux data set based on low resolution ~~observation~~
802 ~~seollected~~ ~~observations collected~~ by the CHAMP satellite between 2000 and 2010,
803 and produced from the MF-6 model following the technique described in Fox

804 Maule et al. (2005), Inter-active System for Ice sheet Simulation [data set],
805 http://webserv.cs.umt.edu/isis/index.php/Antarctica_Basal_Heat_Flux (last access:
806 ~~5 August 2022~~ 11 April 2023), 2012.

807 ~~Reading, A.M., Stål, T., Halpin, J.A., Lösing, M., Ebbing, J., Shen, W., McCormack,~~
808 ~~F.S., Siddoway, C. S., and Hasterok, D.: Antarctic geothermal heat flow and its~~
809 ~~implications for tectonics and ice sheets, *Nat Rev Earth Environ*, 3, 814–831,~~
810 ~~<https://doi.org/10.1038/s43017-022-00348-y>, 2022.~~

811 Roberts, J., Galton-Fenzi, B. K., Paolo, F. S., Donnelly, C., Gwyther, D. E., Padman, L.,
812 Young, D., Warner, R., Greenbaum, J., Fricker, H. A., Payne, A. J., Cornford, S.,
813 Le Brocq, A., ~~van~~Van Ommen, T., Blankenship, D., and Siegert, M. J.: Ocean
814 forced variability of Totten Glacier mass loss, *SP*, 461, 175–186,
815 <https://doi.org/10.1144/SP461.6>, 2018.

816 ~~Rutishauser, A., Blankenship, D. D., Young, D. A., Wolfenbarger, N. S., Beem, L. H.,~~
817 ~~Skidmore, M. L., Dubnick, A., and Criscitiello, A. S.: Radar sounding survey over~~
818 ~~Devon Ice Cap indicates the potential for a diverse hypersaline subglacial~~
819 ~~hydrological environment, *The Cryosphere*, 16, 379–395,~~
820 ~~<https://doi.org/10.5194/te-16-379-2022>, 2022.~~

821 Schroeder, D. M., Blankenship, D. D., and Young, D. A.: Evidence for a water system
822 transition beneath Thwaites Glacier, West Antarctica, *Proc. Natl. Acad. Sci. U.S.A.*,
823 110, 12225–12228, <https://doi.org/10.1073/pnas.1302828110>, 2013.

824 Schroeder, D. M., Blankenship, D. D., Raney, R. K., and Grima, C.: Estimating
825 Subglacial Water Geometry Using Radar Bed Echo Specularity: Application to
826 Thwaites Glacier, West Antarctica, *IEEE Geosci. Remote Sensing Lett.*, 12, 443–
827 447, <https://doi.org/10.1109/LGRS.2014.2337878>, 2015.

828 Shapiro, N. ~~M.~~ and Ritzwoller, M. H.: Inferring surface heat flux distributions guided
829 by a global seismic model: particular application to Antarctica, *Earth and Planetary*
830 *Science Letters, Planet. Sc. Lett.*, 223, 213–224,
831 <https://doi.org/10.1016/j.epsl.2004.04.011>, 2004.

832 Shen, W., Wiens, D. A., Lloyd, A. J., and Nyblade, A. A.: A ~~Geothermal Heat Flux~~
833 ~~Map geothermal heat flux map of Antarctica Empirically Constrained empirically~~
834 ~~constrained by Seismic Structure, *Geophysical Research Letters, seismic structure,*~~
835 ~~*Geophys. Res. Lett.*, 47, e2020GL086955,~~
836 ~~<https://doi.org/10.1029/2020GL086955>, 2020.~~

837 ~~Stearns, L., Stål, T., Reading, A., Smith, B. E. M., Halpin, J. A., and Hamilton, G. S.:~~
838 ~~Increased flow speed on a large East Whittaker, J. M.: Antarctic outlet glacier~~
839 ~~caused by subglacial floods, *Nature Geosci.*, 1, 827–831, geothermal heat flow~~
840 ~~model: Aq1, *Geochemistry, Geophysics, Geosystems*, 22, e2020GC009428,~~
841 ~~<https://doi.org/10.1038/ngeo356>, 2008 1029/2020GC009428, 2021.~~

842 Studinger, M., Bell, R. E., Karner, G. D., Tikku, A. A., Holt, J. W., Morse, D. L., Richter,
843 T. G., Kempf, S. D., Peters, M. E., Blankenship, D. D., Sweeney, R. E., and
844 Rystrom, V. L.: Ice cover, landscape setting, and geological framework of Lake
845 Vostok, East Antarctica, *Earth and Planetary Science Letters, Planet. Sc. Lett.*, 205,
846 195–210, [https://doi.org/10.1016/S0012-821X\(02\)01041-5](https://doi.org/10.1016/S0012-821X(02)01041-5), 2003.

847 Talalay, P., Li, Y., Augustin, L., Clow, G. D., Hong, J., Lefebvre, E., Markov, A.,

848 Motoyama, H., and Ritz, C.: Geothermal heat flux from measured temperature
849 profiles in deep ice boreholes in Antarctica, *The Cryosphere*, 14, 4021–4037,
850 <https://doi.org/10.5194/tc-14-4021-2020>, 2020.

851 Van Liefferinge, B. and Pattyn, F.: Using ice-flow models to evaluate potential sites of
852 million year-old ice in Antarctica, *Clim. Past*, 9, 2335–2345,
853 <https://doi.org/10.5194/cp-9-2335-2013>, 2013.

854 Van Liefferinge, B., Pattyn, F., Cavitte, M. G. P., Karlsson, N. B., Young, D. A., Sutter,
855 J., and Eisen, O.: Promising Oldest Ice sites in East Antarctica based on
856 thermodynamical modelling, *The Cryosphere*, 12, 2773–2787,
857 <https://doi.org/10.5194/tc-12-2773-2018>, 2018.

858 Wolovick, M. J., Moore, J. C., and Zhao, L.: Joint ~~Inversion~~ ~~inversion~~ for ~~Surface~~
859 ~~Accumulation Rates~~ [surface accumulation rate](#) and ~~Geothermal Heat Flow From~~
860 ~~Ice-Penetrating Radar Observations~~ [geothermal heat flow from ice-penetrating](#)
861 [radar observations](#) at Dome A, East Antarctica. Part I: ~~Model Description, Data~~
862 ~~Constraints~~ [model description, data constraints](#), and ~~Inversion Results~~, *JGR*
863 [inversion results](#), *J. Geophys. Res.-Earth-Surface*, 126, [e2020JF005937](#),
864 <https://doi.org/10.1029/2020JF005937>, [2021a.2021](#).

865 ~~Wolovick, M. J., Moore, J. C., and Zhao, L.: Joint Inversion for Surface Accumulation~~
866 ~~Rate and Geothermal Heat Flow From Ice-Penetrating Radar Observations at~~
867 ~~Dome A, East Antarctica. Part II: Ice Sheet State and Geophysical Analysis~~, *JGR*
868 [Earth Surface](#), 126, <https://doi.org/10.1029/2020JF005936>, [2021b](#).

869 Wright, A. and Siegert, M.: A fourth inventory of Antarctic subglacial lakes, *Antarctic*
870 *Science*, 24, 659–664, <https://doi.org/10.1017/S095410201200048X>, 2012.

871 Wright, A. P., Young, D. A., Roberts, J. L., Schroeder, D. M., Bamber, J. L., Dowdeswell,
872 J. A., Young, N. W., Le Brocq, A. M., Warner, R. C., Payne, A. J., Blankenship, D.
873 D., ~~van~~ [Van](#) Ommen, T. D., and Siegert, M. J.: Evidence of a hydrological
874 connection between the ice divide and ice sheet margin in the Aurora Subglacial
875 Basin, East Antarctica, *J. Geophys. Res.*, 117, 2011JF002066,
876 <https://doi.org/10.1029/2011JF002066>, 2012.

877 Young, D. A., Schroeder, D. M., Blankenship, D. D., Kempf, S. D., and Quartini, E.:
878 The distribution of basal water between Antarctic subglacial lakes from radar
879 sounding, *Phil. Trans. R. Soc. A.*, 374, 20140297,
880 <https://doi.org/10.1098/rsta.2014.0297>, 2016.

881 Zhao, C., Gladstone, R. M., Warner, R. C., King, M. A., Zwinger, T., and Morlighem,
882 M.: Basal friction of Fleming Glacier, Antarctica – Part 1: Sensitivity of inversion
883 to temperature and bedrock uncertainty, *The Cryosphere*, 12, 2637–2652,
884 <https://doi.org/10.5194/tc-12-2637-2018>, 2018.

885